Titre: Title:	Impact of Through-Slice Gradient Optimization for Dynamic Slice-Wise Shimming in the Cervico-Thoracic Spinal Cord and the Brain
Auteur: Author:	Arnaud Bréhéret
Date:	2025
Type:	Mémoire ou thèse / Dissertation or Thesis
Référence: Citation:	Bréhéret, A. (2025). Impact of Through-Slice Gradient Optimization for Dynamic Slice-Wise Shimming in the Cervico-Thoracic Spinal Cord and the Brain [Mémoire de maîtrise, Polytechnique Montréal]. PolyPublie. https://publications.polymtl.ca/62514/

URL de PolyPublie: PolyPublie URL:	https://publications.polymtl.ca/62514/
Directeurs de recherche: Advisors:	Julien Cohen-Adad, & Jason Stockmann
Programme: Program:	Génie biomédical

POLYTECHNIQUE MONTRÉAL

affiliée à l'Université de Montréal

Impact of through-slice gradient optimization for dynamic slice-wise shimming in the cervico-thoracic spinal cord and the brain

ARNAUD BRÉHÉRET

Institut de génie biomédical

Mémoire présenté en vue de l'obtention du diplôme de *Maîtrise ès sciences appliquées*

Génie biomédical

Janvier 2025

POLYTECHNIQUE MONTRÉAL

affiliée à l'Université de Montréal

Ce mémoire intitulé :

Impact of through-slice gradient optimization for dynamic slice-wise shimming in the cervico-thoracic spinal cord and the brain

présenté par **Arnaud BRÉHÉRET**

en vue de l'obtention du diplôme de *Maîtrise ès sciences appliquées*

a été dûment accepté par le jury d'examen constitué de :

Eva ALONSO ORTIZ, présidente
Julien COHEN-ADAD, membre et directeur de recherche
Jason STOCKMANN, membre et codirecteur de recherche
Christine Lucas TARDIF, membre

ACKNOWLEDGEMENTS

First and foremost, I would like to thank my director, Julien Cohen-Adad, for giving me this opportunity. From making a 2-month internship in Boston possible to attending an international conference in Singapore, you made these two years an irreplaceable experience, and I am very grateful for it. I would also like to thank you for your mentorship. Even with your busy schedule, you always found time to help and guide me. This helped not only my knowledge of MRI but also my time management, information analysis, communication and technical skills. Next, I would like to thank my co-director, Jason Stockmann, for his valuable advice and generosity. My time in Boston was one of the best experiences in my life, and it would never have been possible without you.

I would like to thank the whole Neuropoly lab for their help and friendship throughout the project, with a special thank you to Alexandre D'Astous for his help with Shimming Toolbox and his many hours passed at the scanner so I could acquire data. A special thanks to Nibardo Lopez-Rios for his help with hardware debugging and his many lessons in electrical engineering.

Finally, I would like to thank my parents, for their unconditional support throughout my academic journey, and my girlfriend Jade for always being there for me, even if it meant reading a whole literature review on a subject she had no prior knowledge of.

RÉSUMÉ

L'objectif de ce mémoire est d'adresser le défi d'homogénéisation du champ B_0 en IRM afin d'améliorer l'imagerie de la moelle épinière et du cerveau à des champs magnétiques élevés (3T et 7T). Les inhomogénéités du champ B_0, responsables de la perte de signal et des distorsions géométriques, posent particulièrement un problème dans la région cervico-thoracique de la moelle épinière et dans le lobe frontal du cerveau en raison des effets de susceptibilité magnétique, des interfaces os-tissus et des mouvements physiologiques. L'objectif de cette recherche est de développer et valider des techniques avancées de *shimming* dynamique tranche-par-tranche afin d'augmenter le signal dans ces régions complexes, en réduisant les gradients dans l'épaisseur de coupe, qui sont la principale cause de perte de signal dans les images écho de gradient.

L'objectif principal est d'évaluer l'impact de l'intégration d'un paramètre (w) dans l'optimisation traditionnelle en moindres carrés (qui minimise le décalage du champ B_0 dans la coupe) afin de concilier deux aspects essentiels : l'homogénéité du champ B_0 dans le plan de coupe et la réduction des gradients dans l'épaisseur de coupe. Cette optimisation, ayant prouvé son efficacité dans le cerveau à 3 Tesla, devrait être encore plus bénéfique à des champs plus élevés (où le déphasage est plus prononcé) et dans la moelle épinière, où l'épaisseur de coupe pour l'imagerie écho-planaire (EPI) est supérieure à celle du cerveau (typiquement 3-5mm).

Pour atteindre ces objectifs, une antenne AC/DC (AC- reçoit le signal; DC – modifie le champ magnétique) à 15 canaux a été développée afin de changer dynamiquement les courants dans l'antenne et donc changer le champ magnétique tranche-par-tranche (DSU) afin de corriger les inhomogénéités. Un groupe de six volontaires sains a passé des examens IRM avec ce système dans un scanner 3 Tesla, permettant des comparaisons entre les acquisitions de référence et le *shimming* dynamique tranche-par-tranche avec différentes valeurs de *w* (0, 0,0001, 0,01 et 1) pour déterminer l'équilibre optimal entre la récupération du signal et l'homogénéité du champ dans la tranche.

Les résultats montrent que l'intégration du paramètre *w* (0,01) dans l'optimisation DSU offre des améliorations substantielles du rapport signal-sur-bruit temporel (tSNR) et de la récupération du signal dans les niveaux ciblés de la moelle épinière, atteignant notamment une amélioration de 201 % au niveau vertébral T2 et de 78 % au niveau vertébral C3. Ces améliorations sont accompagnées de réductions significatives de la racine carrée de l'erreur quadratique moyenne

(RMSE) du champ B_0 et des distorsions géométriques dans le plan. Dans les simulations, le réglage élevé de *w* (*w* = 1) a suggéré que la minimisation des gradients dans l'épaisseur de coupe pourrait théoriquement produire une récupération de signal encore plus importante. Cependant, lors des acquisitions, ce réglage plus élevé s'est révélé instable, entraînant des variations excessives du champ dans le plan et une qualité d'image médiocre en raison de distorsions amplifiées.

L'étude conclut que le *shimming* dynamique tranche-par-tranche avec un paramètre de récupération de signal réglé de manière optimale (*w* = 0,01) offre une solution robuste pour réduire la perte de signal et améliorer la fidélité des images dans la moelle épinière et le cerveau à des champs élevés. Cette approche de *shimming* dynamique améliore les méthodes conventionnelles de *shimming* utilisant les harmoniques sphériques des systèmes IRM et celle qui optimise le volume complet en s'adaptant aux variations complexes du champ présentes dans la moelle épinière, exacerbées par la proximité des poumons et des disques vertébraux.

Les applications de ce travail s'étendent au-delà de l'imagerie de la moelle épinière. En effet, ces techniques de shimming avancées pourraient potentiellement bénéficier à l'IRM fonctionnelle (IRMf) et à l'imagerie en écho de gradient à des champs élevés dans les régions affectées par de forts gradients dans l'épaisseur de coupe et les inhomogénéités du champ B_0, telles que le lobe frontal et la moelle épinière. Les recherches futures pourraient se pencher sur l'intégration d'un suivi du cycle respiratoire en temps réel dans le protocole de *shimming* pour compenser dynamiquement les fluctuations du champ B_0 induites par la variation du volume d'air dans les poumons, stabilisant davantage l'homogénéité du champ au fil du temps et améliorant la récupération du signal dans la moelle épinière et d'autres régions anatomiquement complexes. En outre, des comparaisons avec des systèmes IRM à champ plus élevé (par exemple, 7T) pourraient offrir des perspectives supplémentaires, en particulier dans les régions où les gradients dans l'épaisseur de coupe sont amplifiés par le champ magnétique plus élevé, permettant une compréhension plus complète des stratégies de *shimming* optimales pour différents niveaux de champ.

En somme, ce mémoire contribue à la recherche en l'IRM en présentant un cadre de *shimming* avancé, open-source et adaptable qui améliore les approches actuelles pour l'IRM de la moelle épinière et des champs magnétiques élevés. En intégrant la technologie des antennes AC/DC au *shimming* dynamique tranche-par-tranche, ce travail établit une base pour des

techniques d'IRM améliorées et ouvre la voie à des applications cliniques élargies dans des régions où les inhomogénéités du champ B_0 ont traditionnellement limité la qualité des images.

ABSTRACT

This thesis addresses the challenge of mitigating B_0 inhomogeneities in MRI for improved spinal cord and brain imaging at high magnetic fields (3T and 7T). B_0 inhomogeneities, which cause signal loss and geometric distortions, are particularly problematic in the cervico-thoracic spinal cord and the brain's frontal lobe due to susceptibility effects, bone-tissue interfaces, and physiological motion. This research aims to develop and validate advanced dynamic shimming techniques that can enhance signal recovery in these challenging regions, focusing on reducing through-slice gradients, the principal cause of signal loss in gradient-echo images.

The main objective is to evaluate the impact of incorporating a signal recovery parameter (w) into the traditional least squares optimization (minimizes B_0 offset in the slice) to balance two primary concerns: in-plane B_0 homogeneity and through-slice gradient minimization. Since this optimization has been proven to be helpful in the brain at 3 Tesla, this work hypothesized that this optimization would be even more beneficial at higher field strengths (stronger dephasing), and in the spinal cord where slice thickness for echo planar imaging (EPI) is greater than the brain (typically 3-5mm).

To achieve these objectives, a custom 15-channel AC/DC coil (AC – receive signal; DC – change the magnetic field) was developed to perform dynamic slice-wise shim updating (DSU) for correcting the magnetic field gradients. A group of six healthy volunteers underwent MRI scans using this setup in a 3 Tesla system, with comparisons made between baseline acquisitions, and dynamic slice-wise shimming with different values of *w* (specifically, 0, 0.0001, 0.01, and 1) to determine the optimal balance of signal recovery and field homogeneity.

Results indicate that the incorporation of a moderate *w* parameter (0.01) in the DSU optimization yields substantial improvements in temporal signal-to-noise ratio (tSNR) and signal recovery across targeted spinal cord levels, notably achieving a 201% improvement at T2 and a 78% improvement at C3. Significant reductions in B_0 root mean square error (RMSE) accompanied these enhancements and in-plane geometric distortions. In simulations, the high *w* setting ($w = 1$) suggested that through-slice gradient minimization could theoretically produce even greater signal recovery. However, when applied experimentally, this higher setting proved unstable, resulting in excessive in-plane field variation and poor image quality due to amplified distortions.

The thesis concludes that dynamic slice-wise shimming with an optimally tuned signal recovery parameter ($w = 0.01$) offers a robust solution to reduce signal loss and enhance imaging fidelity in the spinal cord and brain at high fields. This optimized dynamic shim approach improves upon standard spherical harmonics and volume-based shimming methods by accommodating the complex field variations present in the spinal cord, which are compounded by the proximity to the lungs and vertebral discs.

Applications of this work extend beyond spinal cord imaging to potentially benefit functional MRI (fMRI) and gradient echo imaging at high field strengths, where regions affected by through-slice gradients and B_0 inhomogeneities, such as the frontal lobe and spinal cord, could greatly benefit from these advanced shimming techniques. Future work may focus on incorporating real-time respiratory monitoring into the shimming protocol to dynamically compensate for air-variation-induced B_0 field fluctuations, further stabilizing field homogeneity through time and enhancing signal recovery in the spinal cord and other anatomically challenging regions. Additionally, comparisons with higher-field MRI (e.g., 7T systems) could provide further insights, especially in regions where through-slice gradients are amplified by the higher magnetic field, leading to a more comprehensive understanding of optimal shimming strategies across various field strengths.

Overall, this thesis contributes to MRI research by presenting an advanced, open-source, and adaptable shimming framework that improves current approaches for spinal cord and high-field MRI. By integrating AC/DC coil technology with dynamic slice-wise shimming, the work sets a foundation for enhanced MRI techniques and provides a pathway toward broader clinical applications in regions where B_0 field inhomogeneities have traditionally limited imaging quality.

TABLE OF CONTENTS

LIST OF TABLES

LIST OF FIGURES

LIST OF SYMBOLS AND ABBREVIATIONS

A	Anterior
AP	Anterior-Posterior
B0	Main static magnetic field
B1+	Positively rotating RF magnetic field
BET	Brain extraction tool
BOLD	Blood oxygenation level-dependent
BW	Bandwidth
CSF	Cerebrospinal fluid
DC	Direct current
EPI	Echo planar imaging
FA	Flip angle
FMRI	Functional magnetic resonance imaging
FOV	Field of view
GRE	Gradient echo
GUI	Graphical user interface
MRI	Magnetic resonance imaging
MSE	Mean standard error
P	Posterior
PA	Posterior-Anterior
RF	Radiofrequency
RMSE	Root mean squared error
ROI	Region of interest
SCT	Spinal cord toolbox

SH	Spherical harmonics
SNR	Signal to noise ratio
STD	Standard deviation
T	Tesla
T1	Longitudinal relaxation time
T2	Transverse relaxation time
T2*	Effective transverse relaxation time
TE	Echo time
TR	Repetition time
tSNR	Temporal signal to noise ratio
TTL	Transistor-transistor logic

CHAPTER 1 INTRODUCTION

Magnetic resonance imaging (MRI) is a common, non-invasive technique that gives clinicians detailed, high-resolution images of the body, helping them identify lesions, tumours, and other abnormalities [1]–[3]. Its versatility allows for different contrast settings, which makes MRI particularly useful for specialized methods like BOLD functional MRI (fMRI) [4]. However, these advanced techniques are especially prone to issues with magnetic field inhomogeneities, which can lead to image artifacts like shading and blurring [5], as discussed further in the next chapter.

In the case of this study, the most noticeable and problematic artifacts originating from those field homogeneities are signal loss and geometric distortions. These problems, which are already evident at field strengths commonly found in hospitals (1.5T and 3T) are even more pronounced with scanners of higher field strengths (7T and over) [6]. Due to their enhanced signal-to-noise ratio (SNR), these ultra-high-field systems are increasingly available in research settings, making advanced artifact correction techniques essential.

Active shimming, or correcting magnetic field inhomogeneities, is critical for reducing these distortions. Although standard MRI systems include shimming coils that create spherical harmonic fields up to the third order (in some 7T systems), this approach may only provide sufficient homogeneity for some anatomical regions. Others, such as the spinal cord, temporal lobe, and lower frontal lobe, require advanced shimming techniques, further outlined in section 2.3.

Despite the increased complexity of imaging the spinal cord, due to factors like vertebral motion and respiratory effects [7], most advanced shimming research is focused on the brain. A PubMed search, for example, reveals approximately 47,000 articles on spinal cord MRI (keywords — (Spinal cord) AND (MRI)) compared to 322,000 on brain MRI (keywords — (Brain) AND (MRI)), with only 36 spinal cord studies on shimming versus 354 for the brain (Added keyword — Shimming).

This study aims to help address this gap by advancing shimming techniques for spinal cord imaging. Our work is open-source and intended to facilitate further research and development of shimming methods specific to spinal cord applications across research groups.

CHAPTER 2 Literature review

After Isidor Rabi won the Nobel Prize in Physics in 1944 for developing the concept of nuclear magnetic resonance, it took 29 years before Paul Lauterbur acquired the first MRI images [8], [9]. In the early 1980s, the first clinical MRIs were installed and, since then, many advancements have been made in hardware components, image reconstruction, and image analysis [10]. In this chapter, the essential knowledge needed to understand how the magnetic properties of the human body are used to acquire images will be explained, providing a foundation for understanding the challenges in MRI imaging and the various solutions available to address them. Figure 2.1 illustrates the coordinates system used for the rest of the thesis.

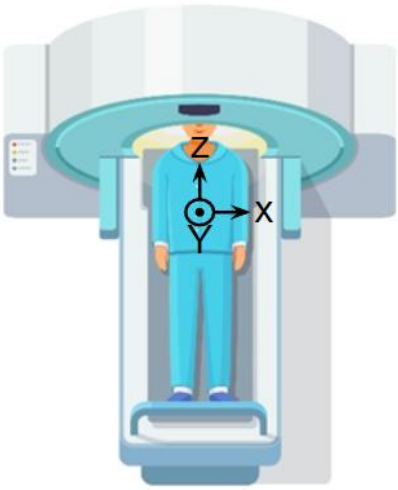

Figure 2.1 MRI scanner and coordinate system.
Image by iconicbestiary on Freepik and modified

2.1 MRI Basics

From the atom to the image, this section will explain the basic principles and important imaging details related to this project.

2.1.1 Spin

The whole basis of MRI imaging revolves around the quantum property of atoms called the spin (I). Depending on their number of protons and neutrons, atomic particles can have null spin, half-integer spin or whole integer spin, as shown in Table 2.1.

Table 2.1 The spin value of an atom

Number of protons	Number of neutrons	Spin (I)
even	even	I = 0
odd	even	I = 1/2, 3/2, …, 15/2
even	odd	I = 1/2, 3/2, …, 15/2
odd	odd	I = 1, 2, …, 8

When a particle has a non-zero spin, it has a magnetic dipole moment μ represented in Figure 2.2 that can interact with electromagnetic fields.

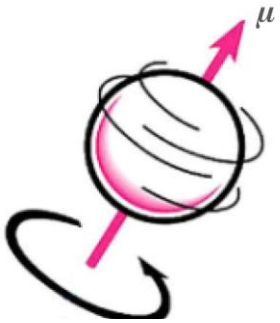

Figure 2.2 Spin and magnetic moment μ. Based on a figure from mriquestions.com, Courtesy of Allen D. Elster, MRIquestions.com

2.1.2 Net Magnetization

When a group of particles with a non-zero magnetic moment is not exposed to any magnetic field, they point in various directions, resulting in a net magnetization (M) of 0. But, when exposed to a magnetic field, these dipoles reach a state called precession. They orient themselves with the field and rotate around its direction, creating 2I + 1 possible states. In the case of hydrogen (I = ½) (see section 2.1.5), there are two possible states: parallel (low energy) or anti-parallel (high energy) to the magnetic field. The sum of these oriented dipoles is not null; as shown in Figure 2.3, a net magnetization (M) is created.

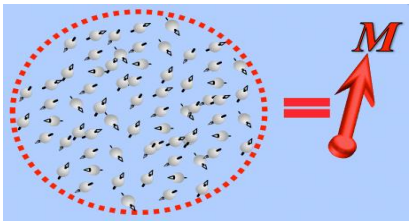

Figure 2.3 Net magnetization created from a group of spins. Courtesy of Allen D. Elster, MRIquestions.com

2.1.3 B_0 Field

MRI's magnetic field is called the main magnetic field or the **B_0 field**. The frequency at which the net magnetization turns around the B_0 field's orientation axis is called the Larmor frequency and is computed using equation 2.1 below.

$$\omega = \gamma B_0 \qquad 2.1$$

$$f = \frac{\omega}{2\pi} \qquad 2.2$$

Where ω is the Larmor frequency in rad/s, γ the gyromagnetic ratio (rad·s^{-1}·Tesla^{-1}) of the particle, B_0 is the main magnetic field (T) and f is the Larmor frequency in Hz.

As γ is specific to the atom, choosing which one you want to image is important. In MRI, hydrogen is the targeted atom. More details in the section 2.1.5.

The next key information to understand is the movement of the magnetic moment around the B_0 field's axis. As shown in Figure 2.4, the magnetic moment vector can be divided into 2 components, one along the field's direction (z) and one in the transverse plane (xy).

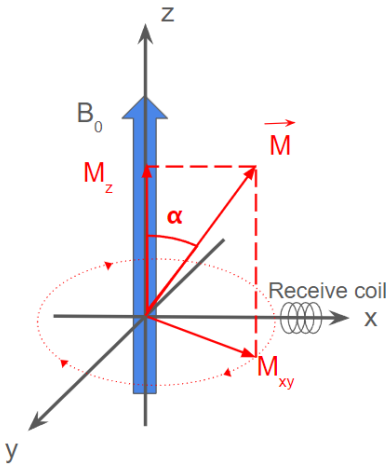

Figure 2.4 Net magnetization in the xyz reference system with its z component M_z and its transverse plane component M_{xy}. The receive coil is placed in the xy plane.

As seen in Figure 2.4, the net magnetization's transverse component varies in time as it turns around the z-axis. According to Faraday's law, a magnetic flux that varies in space or time inside a coil generates current. By adding a coil orthogonal to the xy plane (receive coil in Figure 2.4), the generated current can be used to measure a signal proportional to the transverse magnetization computed with equations 2.3 and 2.4.

$$M_0 = \frac{B_0 \gamma^2 \hbar^2}{4\kappa_B T} P_D \qquad 2.3$$

$$M_{xy}(t) = M_0 \cdot \sin(\alpha) \cdot e^{-i\omega_0 t} \qquad 2.4$$

With M_0 the initial net magnetization, B_0 the main magnetic field strength, γ the gyromagnetic ratio, $\hbar$ Plank's constant, K_B Boltzman constant, T the absolute temperature and P_D the proton density, $M_{xy}(t)$ the rotating transverse magnetization at time t, α the initial angle of the net magnetization vector and the z-axis and ω_0 the Larmor frequency.

From these equations, crucial information needs to be understood: The initial magnetization, and therefore the signal, only depends on the field strength, the temperature, and the proton density. This means different tissues like white and grey matter that have different proton densities will have different signal strengths, creating a contrast and hence, a comprehensible

image. Other key factors affect the image contrast and will be further discussed in section 2.1.6. For the other two parameters, as the temperature must be maintained at a comfortable level for humans, the field strength is the only variable that can be modified to obtain a higher signal. The first MRI images were acquired with magnetic field strengths of around 0.05 to 0.35T, but it wasn't long before most clinical MRIs became 1.5 T scanners [11]. Nowadays, the highest magnetic field achieved on humans is 11.7 Tesla in Paris [12].

The transverse magnetization M_{xy} is affected by one more parameter: the angle between the net magnetization vector and the B_0 axis (alpha). This means that having an alpha of 90 degrees should give the highest signal. This is not entirely true as it also depends on the MRI sequence itself which will be discussed in section 2.1.8. But how can alpha be 90 degrees if the spins align with the B_0 field? A second magnetic field is required: the B_1 field.

2.1.4 B_1 Field

The radiofrequency (RF) field, also called the B_1 field, is applied perpendicularly to the B_0 field. This allows the RF pulse to tip the net magnetization (see Figure 2.5 A) in the transverse plane to obtain a signal. Since the B_1 field strength is much smaller than the B_0 field strength, the overall net magnetic field and the net magnetization amplitude are unchanged. As opposed to B_0, B_1 cannot be static because of the precession of the net magnetization around the B_0 axis. In the same way, the orientation of the push someone gives to a child on a swing depends on where the swing is in its rotation, the RF field rotates at the Larmor frequency to efficiently tip the spins over in the transverse plane as seen in Figure 2.5 B.

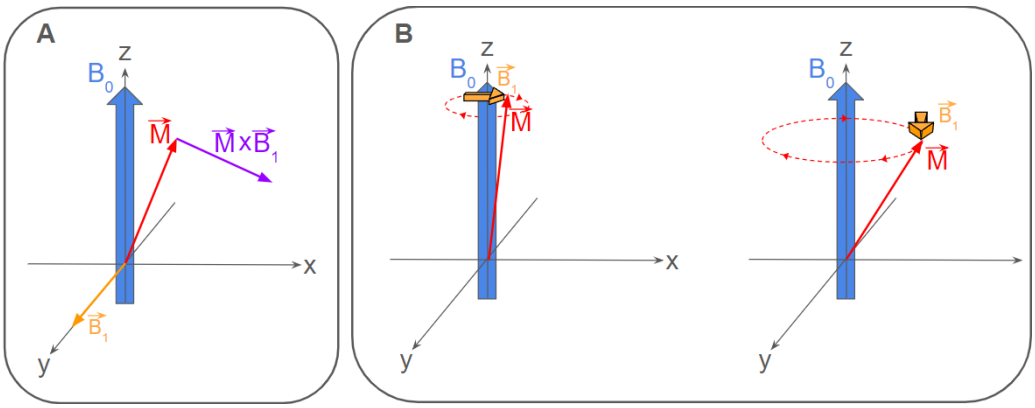

Figure 2.5 (A) Effect of B_1 on net magnetization (M) and (B) Example of B_1 rotating for two different moments.

The resulting flip angle (α) can be computed using equation 2.5.

$$\alpha = \gamma \int_0^{t_e} B_1(\tau) d\tau \qquad 2.5$$

With γ the gyromagnetic ratio, B_1 the radiofrequency field and t_e the excitation time.

Therefore, the flip angle can be modulated with either the B_1 field strength or the excitation time. This gives a degree of freedom that can be highly useful when it comes to creating a new sequence (see section 2.1.8). The last key detail to extract from this equation is that the resulting flip angle also depends on the gyromagnetic ratio, a parameter unique to an atom. This means only one population of atoms can be imaged at a time and with many possible options in the human body, which one to choose?

2.1.5 Why Hydrogen?

In MRI the atom of choice is hydrogen for many different reasons. First, hydrogen only has one proton and zero neutron, resulting in a spin state of ½, hence it can be imaged. Second, hydrogen is the most common atom in the human body. It is found in water (H_2O) and fat, which compose most of human tissues. Consequently, exciting hydrogen atoms allow us to image most of the human body. Lastly, hydrogen happens to have favourable magnetic properties. It has a large magnetic moment relative to other nuclei and its ½ spin state simplifies the understanding of its magnetic resonance.

2.1.6 Relaxations

The measured signal decays after applying the radiofrequency field because the spins interact with themselves and their environment. This phenomenon is named relaxation and can be divided into two different types: T_1 and T_2.

2.1.6.1 T_1 Relaxation

As the B_0 is static and constant, once the spins are flipped in the transverse plane, they naturally return to being aligned with the main magnetic field. This return to their original position is called the **T_1 relaxation** or longitudinal relaxation. The longitudinal net magnetization (M_z) recovery across time during the T1 relaxation can be computed using equation 2.6 below.

$$M_z = M_0\left(1 - e^{-\frac{t}{T_1}}\right) \qquad 2.6$$

With M_z the longitudinal net magnetization, M_0 the initial magnetization when M is aligned with the B_0 field, t the time and T_1 the relaxation constant, approximately 63% of M_0.

This equation is illustrated in Figure 2.6 below.

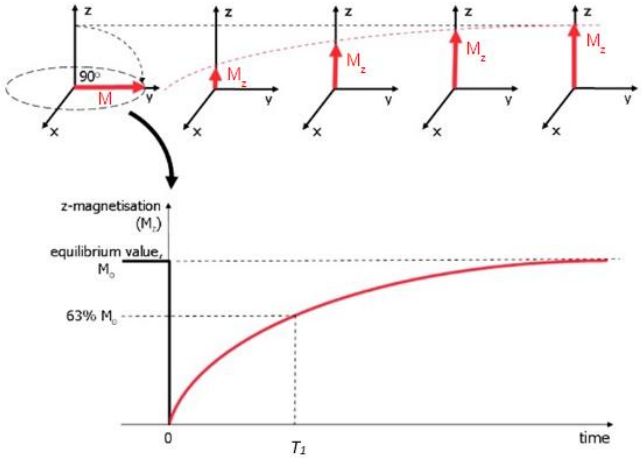

Figure 2.6 Evolution of the longitudinal component of the net magnetization across time after RF excitation. Adapted from course GBM8378 at Polytechnique Montreal.

The T_1 relaxation constant is different for every tissue. For example, at 1.5T, T_1 constants for gray matter and cerebrospinal fluid (CSF) are 900 ms and 4000 ms respectively [13]. This characteristic of tissues can be exploited (just like proton density in section 2.1.3) to obtain a different contrast in images. As demonstrated in Figure 2.7, if you flip the net magnetization vector in the transverse plane, wait 2000 ms and measure the longitudinal magnetization (M_z) for both gray matter and CSF, the gray matter will have a higher M_z, even if CSF has a higher proton density. Hence, if you flip the spins again at that time, the gray matter will have a higher transverse magnetization (M_{xy}), resulting in a higher signal. This characteristic is exploited in what are called T1w imaging sequences like MPRAGE, described in more detail in section 2.1.8.4.

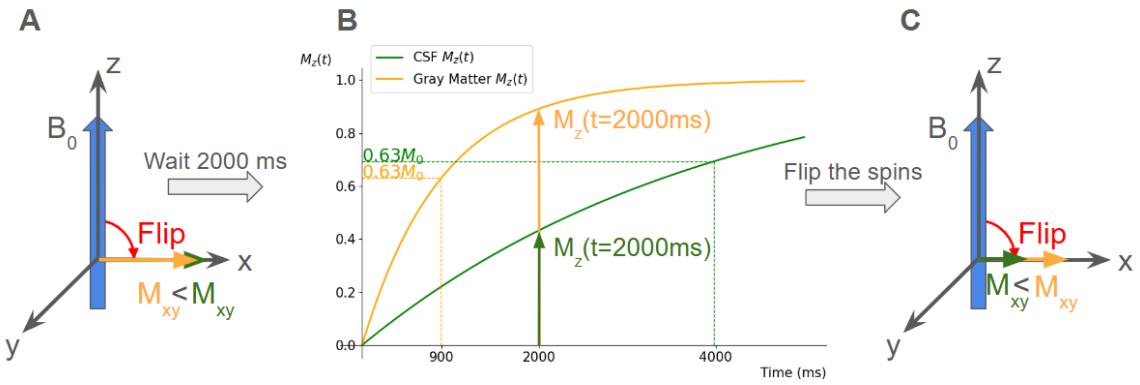

Figure 2.7 Example of the steps to obtain a T_1w contrast. (A) Green and orange magnetization are first flipped into the xy plane. (B) Their M_z component regains magnitude from the T1 relaxation and (C) the Mz component is then flipped again into the xy-plane.

2.1.6.2 T_2 and T_2* Relaxation

Transverse relaxation, also known as T_2 relaxation, is the process by which the transverse magnetization M_{xy} decays due to spin dephasing. The interactions between the spins change the frequency at which spins process, dephasing the spins between each other and, hence reducing the acquired signal.

Spin dephasing can also be caused by B_0 field inhomogeneities created by other factors than the tissues themselves. The causes of those inhomogeneities are discussed in section 2.2.1. As seen in equation 2.1 if B_0 changes, so does the frequency at which the spins process. Therefore, spins dephase at an even greater rate than expected by T_2 decay. This greater decay is called effective decay or T_2* decay and is shown in Figure 2.8.

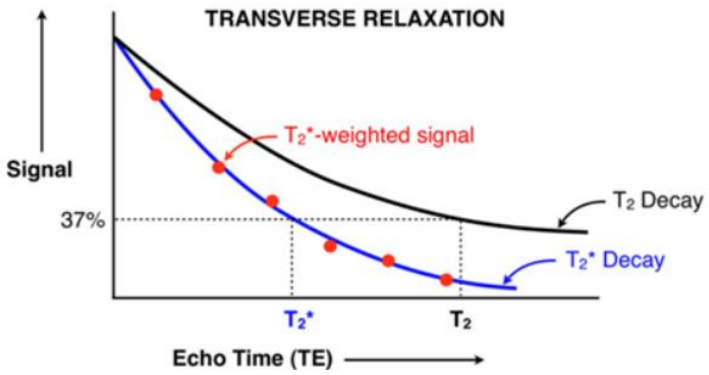

Figure 2.8 T_2 vs T_2* signal decay. From course GBM8378 at Polytechnique Montreal.

Coming back to equation 2.4, a new term can be added to consider T_2^* decay.

$$M_{xy}(t) = M_0 \cdot \sin(\alpha) \cdot e^{-i\omega_0 t} \cdot e^{-\frac{t}{t_2^*}} \quad 2.7$$

$$\frac{1}{T_2^*} = \frac{1}{T_2} + \frac{1}{T_2'} \quad 2.8$$

With $M_{xy}(t)$ the rotating transverse magnetization at time t, α the initial angle of the net magnetization vector and the z-axis, ω_0 the Larmor frequency, T_2 the transverse relaxation constant, T_2* the effective transverse relaxation constant and T_2' the contributions from the field inhomogeneities on the decay.

Just like T_1, T_2 is specific to tissues and consequently can be used to create contrast in an image. Waiting longer after flipping the spin in the transverse plane with the B_1 field will make the signal from two different tissues different. For example, if tissue A has a T_2 decay identical to the one shown in Figure 2.8 and tissue B has a T_2 identical to T_2* shown in the same figure, at time T_2, the acquired signal would show tissue A as a high signal and tissue B as a very low signal.

2.1.7 Image Encoding and Gradients

Previous sections provided all the necessary knowledge to acquire an MR signal but still missed one key information on obtaining an image from it: How do you know where the signal came from? Using previous information, receive coils would acquire a single signal function composed of all sinewaves produced by all the spins in the ROI to create a one-pixel image. This

section will explain the two methods used to obtain an image with a desired resolution: frequency encoding and phase encoding.

2.1.7.1 Frequency Encoding

Frequency encoding is maintaining a magnetic field gradient to change the spin rotating frequency linearly in a direction (x, y, z). This allows for two things.

First, in a 2D imaging sequence where you divide your volume into multiple slices and image one slice at a time, a frequency encoding gradient can be used so each slice has its spins rotating at a different frequency than the other slices (see Figure 2.9 A). As discussed in section 2.1.4, the B1 field excites spins at a specific frequency. Hence, by using an RF pulse with a specific frequency bandwidth, each slice can be excited separately with the desired slice thickness. The same principle can be applied to excite different chemical species like fat instead of water.

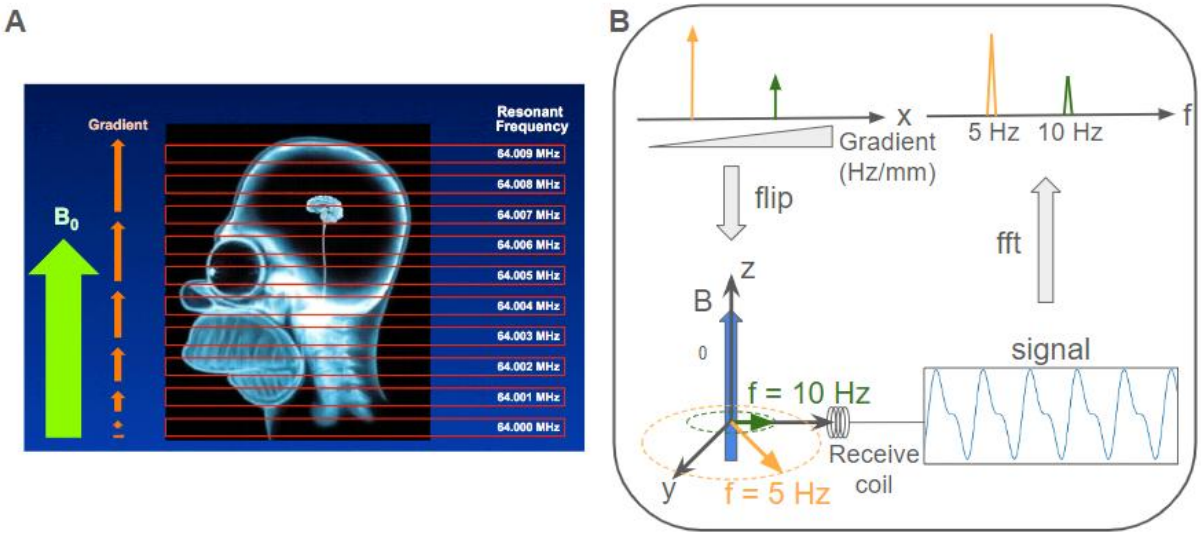

Figure 2.9 Frequency encoding for (A) Slice selection and (B) spatial encoding. (A) Courtesy of Allen D. Elster, MRIquestions.com

The second use of frequency encoding is spatial encoding and is illustrated in Figure 2.9 B. By adding a gradient in one of the slice's directions, spins within the slice will spin at a different frequency. The acquired signal can then be separated in its frequency contributions using a Fourier transform. This is enough to encode a 1D image (line) spatially, but MRI images have slices in 2D. In this case, frequency encoding is insufficient, and phase encoding is added.

2.1.7.2 Phase Encoding

Phase encoding is applying a linear gradient for a short time to make spins out of phase with each other. Since applying a linear gradient will change the frequency of the spins in one direction, once the gradient is removed, the spins return to their original frequency but keep a phase memory. Therefore, the spins in the direction where the gradient was applied process at the same frequency but are out of phase from each other. In combination with frequency encoding, phase encoding allows for spatial encoding, mapped by a grid called the k-space.

2.1.7.3 K-space

K-space is the spatial frequency map and the acquired image's Fourier transform. In MRI, k-space is measured using frequency and spatial encoding to navigate it. A 2D or 3D Fourier transform is then applied to reconstruct the image.

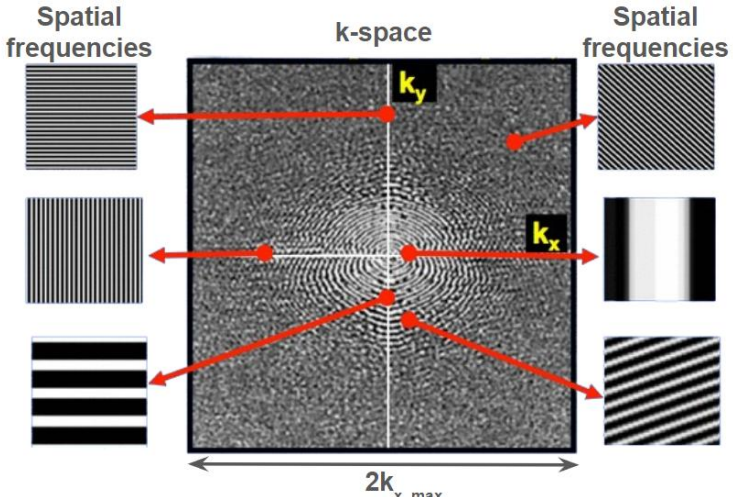

Figure 2.10 K-space with examples of spatial frequencies.
$k_{x,max}$ is in 1/m.
Courtesy of Allen D. Elster, MRIquestions.com

Each point in the Figure 2.10 represents the weights of the different spatial frequencies and adding every spatial frequency together gives the image. The resolution of the resulting image can be computed using equations 2.9 and 2.10.

$$2k_{x,max} = N_x \cdot \gamma \cdot G_x \cdot T, \qquad 2k_{y,max} = N_y \cdot \gamma \cdot G_y \cdot T \tag{2.9}$$

$$\Delta x = \frac{1}{2k_{x,max}}, \qquad \Delta y = \frac{1}{2k_{y,max}} \tag{2.10}$$

$$FOV_x = \frac{1}{\Delta k_x}, \qquad FOV_y = \frac{1}{\Delta k_y} \tag{2.11}$$

Where $k_{max,}$ (1/m) is the highest positive spatial frequency, N is the number of points, gamma is the gyromagnetic ratio (rad/T/s), G is the gradient (T/m), T is the acquisition time (s), Δx/Δy is the image's pixel width and FOV is the image size.

These equations illustrate how the MRI operator needs to consider a balance between the image's FOV and resolution, and how a stronger gradient can provide a higher resolution image or the same resolution image in a shorter time.

To navigate and acquire k-space, different trajectories are possible (see section 2.1.8.1 and 2.1.8.3 for an example).

2.1.8 Basic Sequences

As briefly discussed in previous sections, MRI can be used in various ways. From different contrasts to the measure of blood oxygenation, many valuable images can be acquired from the same technology. To achieve these various possibilities, different imaging sequences must be employed. This section will explain the most useful sequences for this project to better understand their use and role in the research from this thesis.

Before going forward, some concepts need to be defined. RF refers to a radiofrequency pulse or the B1 field explained in section 2.1.4. The time between two RF pulses is called repetition time (TR) and the time between the RF pulse and the signal acquisition is called echo time (TE). Those parameters affect the acquired signal. A long TR allows the spins to regain their original state, favouring proton density contrast. A short TE reduces the impact of T_2 relaxation while a long TE allows for a better separation between two tissues with different T_2 relaxation rates. Figure 2.11 illustrates the different contrasts acquired with different parameters.

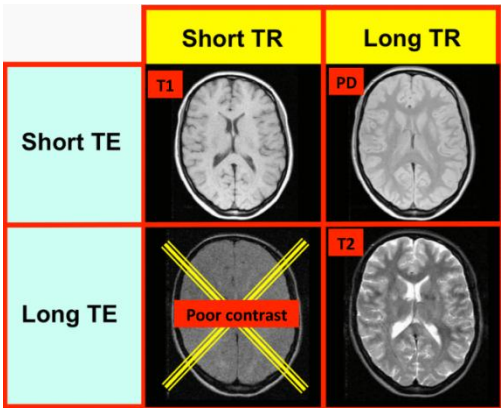

Figure 2.11 Different contrasts and the different parameters needed to achieve them. Courtesy of Allen D. Elster, MRIquestions.com

2.1.8.1 Gradient Echo

Gradient echo (GRE) is the term used to describe the acquisition of signal produced by dephasing and then rephasing the spins using the frequency encoding gradient. An example of a 2D GRE sequence to acquire one line of k-space is shown in Figure 2.12. Lines of k-space are acquired in order from A to I by repeating the sequence.

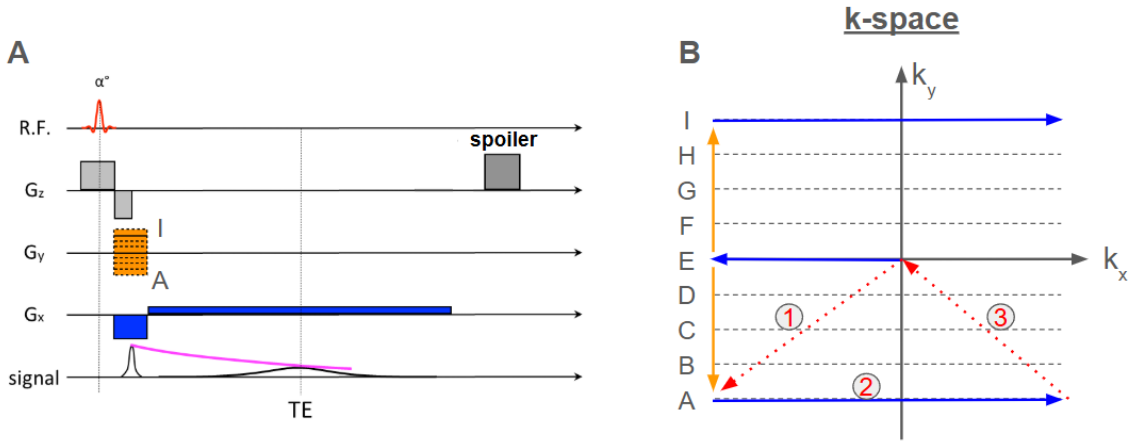

Figure 2.12 Example of a (A) 2D GRE sequence for one line of k-space and (B) the k-space trajectory. In this example, G_z is used as a slice encoding gradient, G_y for phase encoding and G_x for frequency encoding. The orange arrows in (B) represent the effect of G_y and the blue arrows the effect of G_x. (A) Adapted from course GBM8378 at Polytechnique Montreal.

As seen in the figure above, the spins are dephased by the first G_x gradient and are then rephased by the second G_x gradient. At time TE, the spins are back in phase, hence the peak in signal. The rephasing gradient corrects the dephasing induced by the first gradient but cannot correct the dephasing caused by the B_0 inhomogeneities. Therefore, the signal decays following T_2* relaxation. By changing TR and TE according to Figure 2.11, the different contrasts can be achieved using a GRE sequence (T_2 is replaced by T_2* for GRE).

2.1.8.2 Field Map

GRE sequences can also be used to assess the state of the B_0 field. By repeating the dephasing/rephasing of the spins using the G_x gradient in Figure 2.12, multiple echoes can be acquired at a higher echo time. Since the signal can be decomposed in magnitude and phase, the phase difference can be used to compute the offset precession frequency.

$$Signal = RE + i \cdot Im \tag{2.12}$$

$$\phi = \arctan\left(\frac{Im}{Re}\right) \tag{2.13}$$

$$\omega_{offset} = \frac{\phi_2 - \phi_1}{TE_1 - TE_2} \tag{2.14}$$

Where RE and Im are the real and imaginary parts of the signal, ϕ_i the phase at echo time i, TE_i echo time i and ω_{offset} the offset frequency. For example, at 3T, the Larmor frequency is 127.74 Mhz. ω_{offset} is the difference between this frequency and the frequency of the spins in a specific voxel (3D pixel). An example of a dual-echo GRE is displayed in Figure 2.13.

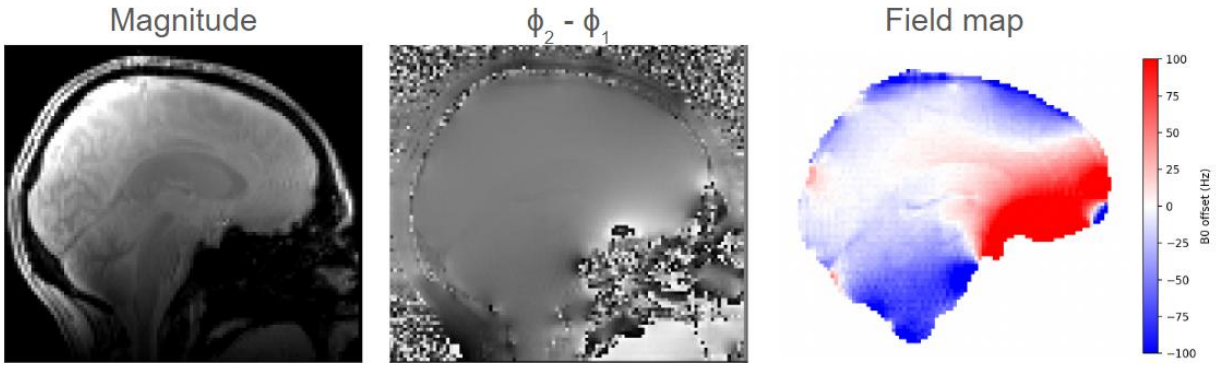

Figure 2.13 Magnitude, phase difference (ϕ_1 -ϕ_2) and field map for a sagittal slice of a brain imaged at 7T

Note that the phase was unwrapped before the phase difference. Phase wraps come from the phase being computed between 0 and 2π, meaning a phase of 3π would appear as π. Phase unwrapping consists of computing the true phase value and, therefore, removing the 0 to 2π range.

These field maps are handy for measuring B_0 inhomogeneities and therefore correcting them. The cause of those inhomogeneities and how to correct them will be further discussed in section 2.2 and 2.3 respectively.

2.1.8.3 Echo-planar Imaging

Echo-planar imaging (EPI) is a k-space trajectory that allows the filling of the whole k-space in one TR. Compared to the normal k-space trajectory shown in the previous section where one line of k-space is acquired after every RF pulse, EPIs adopt a zig-zag trajectory, allowing for a much faster acquisition. Figure 2.14 shows an example of a GRE-EPI sequence (A) to fill one 2D k-space (B).

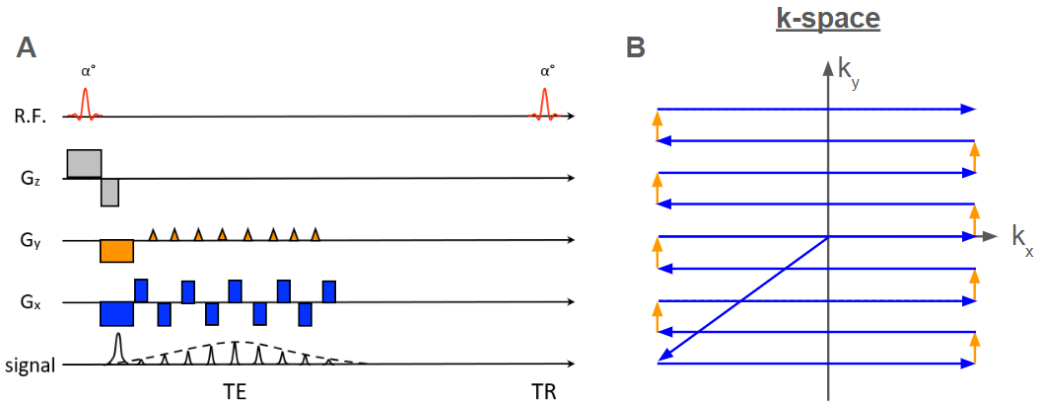

Figure 2.14 GRE-EPI (A) sequence and (B) k-space trajectory with the orange arrows corresponding to the effect of the G_y gradient and the blue arrows to the effect of the G_x gradient. (A) Adapted from course GBM8378 at Polytechnique Montreal.

The figure above shows that not every k-space line is acquired at the optimal signal peak (TE). This reduces the overall signal compared to acquiring one k-space line at a time where every line is acquired at TE. Multi-shot EPI sequences limit this effect by dividing a 2D k-space into multiple zig-zag acquisitions, requiring more RF pulses. Although the faster acquisition reduces

the signal, it also reduces motion effects and gives higher temporal resolution, allowing time series image analysis like functional imaging (fMRI).

2.1.8.4 MPRAGE

Magnetization Prepared – Rapid Gradient Echo (MPRAGE) is a 3D T_1w gradient echo sequence. Using a short echo time limits the effects of B_0 inhomogeneities, making this sequence particularly useful for obtaining a detailed image of your region of interest (ROI).

2.2 B_0 Field Inhomogeneities and Artifacts

As briefly discussed in the section 2.1.6.2, the main magnetic field is not homogenous like the equations assume. The B_0 inhomogeneities create different artifacts, particularly in T_2*-weighted images. This section will discuss the sources of those inhomogeneities and the artifacts they create.

2.2.1 Sources of B_0 Inhomogeneities

Apart from hardware variability (e.g. The magnet does not produce a perfect magnetic field), the principal sources of inhomogeneities come from in-vivo/physiological behaviours that cannot be avoided. Those sources have a lot more impact than hardware at high field strength, making them the principal sources of artifacts.

2.2.1.1 Magnetic Susceptibilities

Magnetic susceptibility (χ) describes the magnetization of a material when placed in an external magnetic field. Materials with a negative susceptibility ($\chi < 0$) are called diamagnetic, while positive susceptibility materials ($\chi > 0$) are called paramagnetic, superparamagnetic, or ferromagnetic according to how high their susceptibility is. For example, air is paramagnetic, while metals are ferromagnetic. Most of the biological tissues in the body are diamagnetic, with bones having the highest negative susceptibility. The susceptibility itself does not create any issue, but the change in susceptibility does, as seen in Figure 2.15.

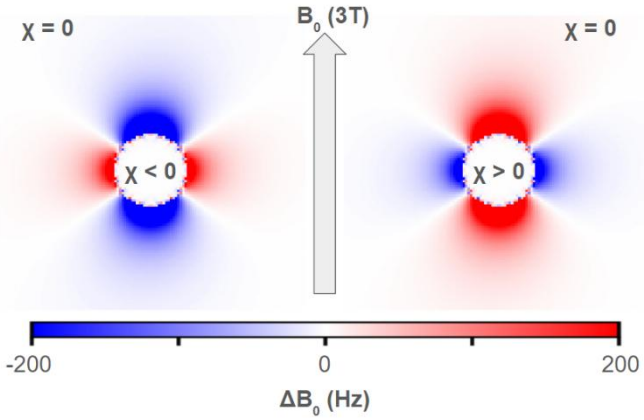

Figure 2.15 B_0 field variations from a circle with $\chi < 0$ and $\chi > 0$ inside a 3T magnetic field.

The B_0 inhomogeneities are directly proportional to the magnetic field. Therefore, a higher magnetic field allows for better SNR but also comes with more artifacts from inhomogeneities. Correcting those inhomogeneities is crucial when working with higher field strength.

An example of a brain field map at 7T was shown in Figure 2.13. The field demonstrates the impact of the sinuses (filled with air -- paramagnetic) in proximity with brain tissues (diamagnetic) creating a strong positive B_0 offset (red region) in the frontal lobe.

2.2.1.2 Breathing

An important distinction that should be considered is the difference between static and dynamic B_0 variations. Most inhomogeneities come from static variations in magnetic susceptibility (i.e. the different non-moving tissue in the human body), but some organs like the lungs and the heart are dynamic. The most impactful physiological movement for spine imaging is breathing. When the lungs expand and retract, the interface between air and tissue changes, hence the field changes. These variations have been studied and characterized [14], [15], illustrating a field variation that follows the breathing cycle. In addition, they are greater in areas close to the lungs, making thoracic spinal cord imaging particularly difficult. Breathing also induces movement, which creates motion artifacts.

2.2.2 Impact of B_0 Inhomogeneities

Some concepts explained previously like k-space trajectory assumed a perfect B_0 field. As this assumption is necessary for some sequences, different artifacts occur. This section describes and illustrates the two principal artifacts seen in 2D GRE-EPI images, the sequence of interest during this project.

2.2.2.1 Geometric Distortions

Geometric distortions appear in EPI images due to k-space trajectory. As explained in the section 2.1.8.3, EPI sequences fill the k-space using a zigzag trajectory. If the field in the imaging region contains inhomogeneities, spin dephasing occurs. This leads to a different k-space trajectory, as shown in Figure 2.16 below. Since the mathematics behind it considers the theoretical trajectory, the image is reconstructed using a false k-space, leading to distortions in the phase encoding direction.

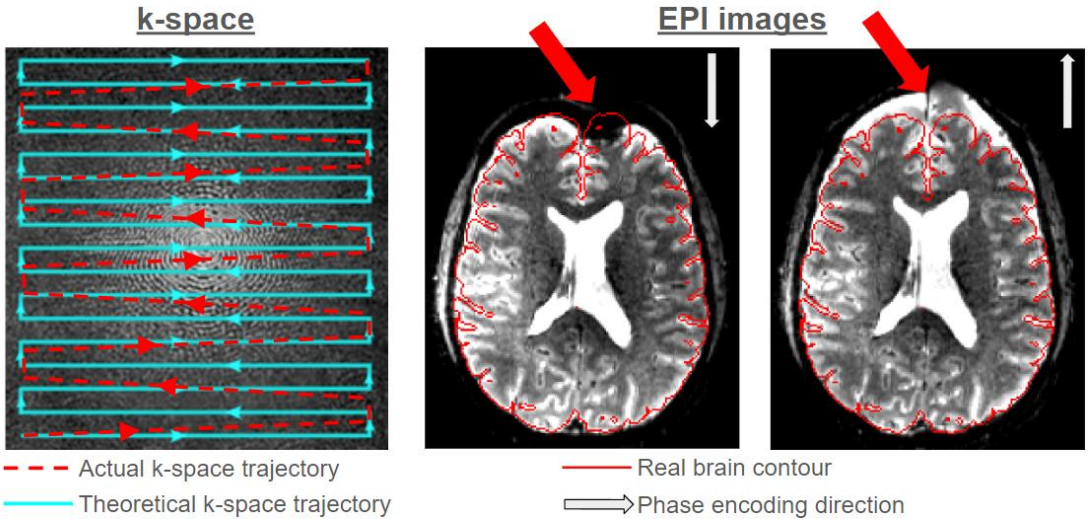

Figure 2.16 Impact of k-space trajectory and phase encoding direction on EPI images.

2.2.2.2 Signal Loss

In MRI imaging, it is impossible to image every single spin individually. The anatomy of interest needs to be imaged with a specific resolution (e.g. 1x1x1 mm). Each cube imaged is called a voxel (3D pixel) and contains multiple spins. In the previous field map shown in Figure 2.13, the

B_0 offset is computed for each voxel, but that does not mean that each spin within this voxel process at the computed frequency, only the average of all the spins in the cube does. A common assumption is that the field varies linearly. This means the spins within the same voxel dephase from one another, which induces signal loss. This phenomenon is the source of T_2* decay. Some sequences like a spin-echo EPI that uses an additional RF pulse can remove this effect and obtain a T_2-weighted image instead of T_2*. Since the field varies linearly with a voxel, the bigger the voxel is, the bigger the field change is, the bigger the dephasing is and hence the more signal is lost. This is particularly a problem while imaging regions that require high in-plane resolution to delineate small structures (e.g. spinal cord) because they require thick slices for sufficient SNR [16].

2.3 Shimming

Shimming is the process of homogenizing the magnetic field. It can either be passive or active.

2.3.1 Passive vs Active Shimming

Passive shimming refers to the action of shimming without the use of currents. It can be done using metal sheets or any ferromagnetic material to modify the magnetic field. Although it is typically done to shim the magnetic field of a new scanner to make sure the B_0 field is homogeneous to a satisfactory degree of precision without a subject in the bore, some groups have tried intra-oral passive shimming [17], [18]. This technique is hard to implement on a subject-specific basis, hence why active shimming is usually the solution of choice.

Active shimming is the process of changing the magnetic using currents. A magnetic field is generated by passing current through wire windings according to Faraday's law. Since the B_0 field can be mapped (as seen previously in section 2.1.8.2), this technique is prevalent to proactively shim the magnetic field for each subject. By minimizing the B_0 offset in the field map, one can compute the optimal current to use in each loop of his coil to obtain the best possible field and therefore, the best possible image.

2.3.2 Coils

This subsection will present the different types of coils that have been developed for MRI active shimming purposes. Note that each of these coils can be mapped using field maps to profile the field change induced by each current unit added into a loop. The result of this process is called coil profiles.

2.3.2.1 Spherical Harmonic Coils

Spherical harmonic coils are coils which generate a magnetic field described by spherical harmonics (see Figure 2.17), which are all orthogonal to each other (distinct magnetic field patter that do not interfere with each other). Commercial scanners usually have spherical harmonics up to second-order [19] and some even have coefficients of the third order. Usually, research groups only use spherical harmonics available on their scanners, but some groups created custom higher-order spherical harmonic insert coils [20].

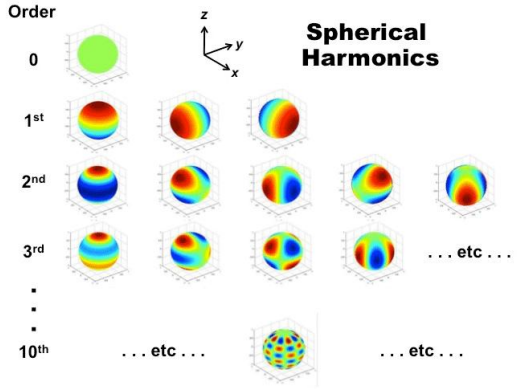

Figure 2.17 Spherical harmonics. Courtesy of Allen D. Elster, MRIquestions.com

2.3.2.2 External Multi-coils

External multi-coils (MC) are a set of loops that generate non-orthogonal B_0 magnetic fields to each other. The number of loops depends on the coil [21]–[23] and the more loops there are, the more complex the generated magnetic field can be. Their advantage over spherical harmonics is their proximity to the imaged region and their ability to be made and optimized for specific anatomy like the brain or the spine. The problem with these types of coils is the extra space they take inside

the bore and the limited positioning of the loops because of the space the receive coil uses [19]. This is why AC/DC or iPRES coils were built.

2.3.2.3 AC/DC Coils

AC/DC [24] or iPRES [25] coils are radiofrequency (AC) and shim (DC) coils. Each loop in these coils can shim, receive, transmit or a combination of those three, reducing the amount of space necessary by combining the receive (and sometimes transmit) coil with the multi-coil. The shim loops can also be closer to the region of interest, allowing for better shims. An example of an AC/DC coil [26] with the magnetic field generated by 3 loops is shown in Figure 2.18.

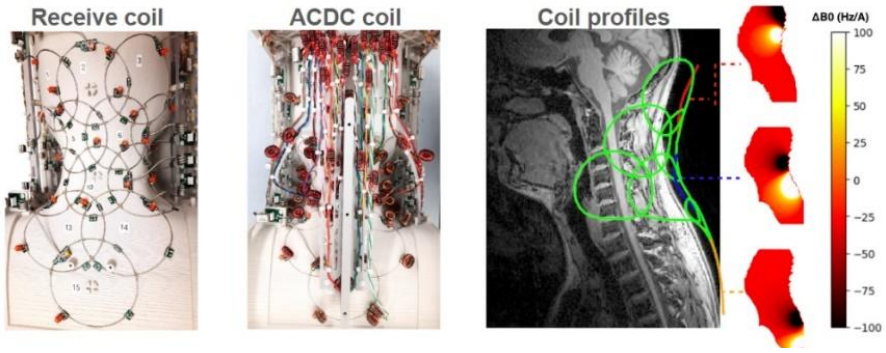

Figure 2.18 Transformation of a receive coil into an ACDC coil with the coil profiles for 3 channels. Coil built by Nibardo Lopez-Rios [26].

2.3.3 Shimming Methods

Whatever shim coil is chosen, how it is used drastically affects the B_0 field improvement. By acquiring a B_0 field map at the beginning, one can measure the B_0 inhomogeneities. Knowing the field change each coil produces (coil profiles), the currents in each loop can be optimized to minimize different criteria (root mean squared error, standard deviation, etc). This subsection will present the three main shimming methods currently used in the field.

2.3.3.1 Volume Shimming

Volume shimming is the most basic and easy-to-use method. It consists of optimizing the currents/coefficients for each loop and/or spherical harmonics for the whole volume of interest

(VOI). This technique works well with small VOIs or larger VOIs with a low amount of field variations. Volume shimming is implemented in most scanners for their spherical harmonics coils and is used before most scans. If the VOI is larger to a point where there are many field variations, like in the spinal cord, slice-wise shimming is better suited to compensate for the inhomogeneities.

2.3.3.2 Slice-wise Shimming

Slice-wise shimming is a technique that can be used in 2D sequences to shim each slice of the volume individually. As 2D sequences acquire the VOI in smaller parts (slices), the optimization can be computed for each slice individually and provide a more tailored shim to each acquired slice (see Figure 2.19). This is not used by every research group because having different currents and/or coefficients for every slice means they need to be changed during the acquisition itself. This needs sequence programming and/or advanced shimming hardware. Ever since the first slice-wise shimming experiments using the scanner's spherical harmonics [22], [27] which showed the limitation of higher-order spherical harmonics to be changed rapidly, some research groups followed with multi-coils [21], [28]–[30], AC/DC coils [31], [32], iPRES coils [33]–[36] and custom higher-order spherical harmonic insert coil [20].

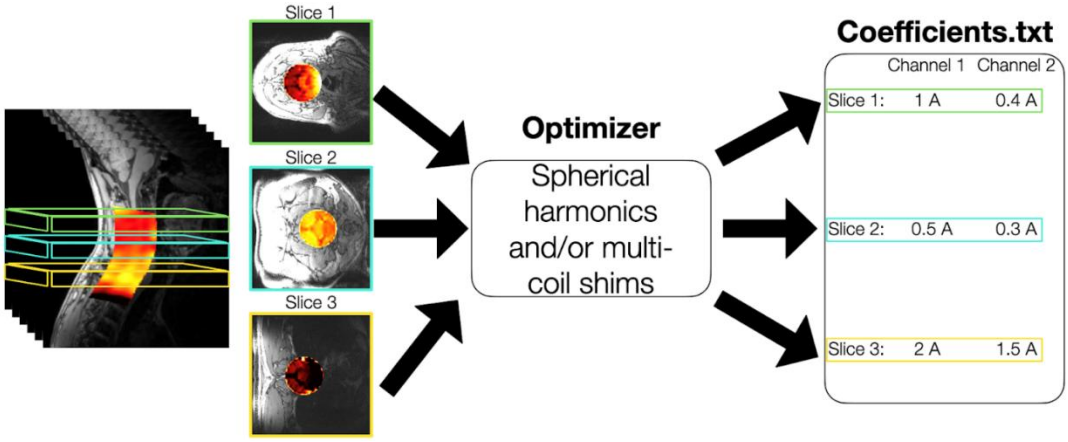

Figure 2.19 Dynamic slice-wise shimming optimization example using three slices and two shim channels. Each slice is sent to the optimizer which returns one set of coefficients for each slice.

2.3.3.3 Real-time Shimming

Real-time shimming refers to shimming the B_0 field variations occurring during the acquisition. As previously mentioned in section 2.2.1.2, physiological events like breathing can

cause field variations that are not accounted for by a simple field map at the beginning of the acquisition. Staying with the example of breathing, shimming in real-time its effect requires monitoring the subject's breathing cycle with a pressure probe, acquiring a B_0 field map at different moments in the cycle and correlating the time-varying field variations with the breathing cycle. Then, a new optimization term called RIRO (Respiratory-Induced Resonance Offset) can be computed, as seen in equation 2.15.

$$\Delta B_0(t) = \Delta B_{0,static} + RIRO \cdot P(t) \qquad 2.15$$

Where $\Delta B_0(t)$ is the total field offset at time t, $\Delta B_{0,static}$ is the static field offset (i.e. induced by different susceptibilities), RIRO is the offset induced by breathing and P(t) is the pressure at time t.

Using this equation, by measuring the pressure before every slice, the slice-wise shim can change currents according to the subject's position in his breathing cycle. This shimming technique has been done with the scanner's gradients [37] and with a multi-coil array [23].

CHAPTER 3 Thesis premise

The literature review provided insights into the fundamentals of MRI, particularly in understanding how B_0 inhomogeneities contribute to imaging issues. These inhomogeneities are especially prevalent in the spinal cord, where the complex interface between vertebral bones, intervertebral discs, and surrounding tissues creates significant static field variations [7], [38]. Combined with dynamic field changes and movement from breathing, the spinal cord presents one of the most challenging environments for MRI. Additionally, the spinal cord's small cross-section requires high in-plane resolution for GRE-EPI sequences [39]. To maintain adequate SNR, this high resolution is typically paired with a thicker slice, which amplifies signal loss in gradient-echo acquisitions.

To address this issue, Finsterbusch et al. diverged from the conventional optimization approach, which primarily minimizes field offset measured by a field map. Instead, they acquired EPIs with varied z-gradients [16], [40]. By selecting the optimal z-gradient for each slice, they achieved notable signal improvements by adjusting the z-gradient dynamically for subsequent slices. While effective, this method has limitations: first, it requires testing multiple z-gradients for each slice, which, although manageable for z-gradient optimization, is impractical for expanding to higher-degree-of-freedom shimming solutions such as multi-coils and AC/DC coils. Second, this optimization is based on the final image rather than directly on the B_0 field, meaning it cannot account for field variations induced by breathing.

In brain imaging, a more recent method—signal recovery optimization—addresses these challenges by incorporating an additional term to jointly optimize in-plane B_0 homogeneity and the through-slice gradient [35]. This advancement in brain imaging has inspired the main objective of this project.

3.1 Main Objective

Evaluate the impact of signal recovery optimization in the cervicothoracic spinal cord and the brain using AC/DC coils and open-source solutions.

3.2 Sub Objectives

SO1: Fix and implement the open-source shimming system [41] for the 3T scanner at UNF.

SO2: Help complete the 15-channel AC/DC coil.

SO3: Program dynamic slice-wise shimming on the Teensy in the shimming software.

SO4: Program a Shimming-Toolbox-compatible interface to allow communication between the user's computer and the shimming system.

SO5: Implement dynamic slice-wise shimming on the scanner (add TTL triggers to sequences) and lead shimming experiments using this new method.

SO6: Implement signal recovery optimization on the Shimming Toolbox software.

SO7: Create a protocol to study and evaluate the impact of signal recovery optimization in the spinal cord and the brain.

The completion of all seven sub-objectives in the spinal cord led to the creation of the article presented in the next section.

CHAPTER 4 Article 1: Impact of through-slice gradient optimization for dynamic slice-wise shimming in the cervico-thoracic spinal cord

Journal - Submitted to Magnetic Resonance in Medicine on 2024-12-04

Arnaud Breheret[1], Alexandre D'Astous[1,2], Jason P. Stockmann[3,4], Julien Cohen-Adad[1,2,5,6]

1: NeuroPoly Lab, Institute of Biomedical Engineering, Polytechnique Montréal, Montréal, QC, Canada

2: Centre de recherche du CHU Sainte-Justine, Université de Montréal, Montréal, QC, Canada

3: Athinoula A. Martinos Center for Biomedical Imaging, Massachusetts General Hospital, Charlestown, MA, United States

4: Harvard Medical School, Boston, MA, United States

5: Functional Neuroimaging Unit, CRIUGM, Université de Montréal, Montréal, QC, Canada

6: Mila - Quebec AI Institute, Montréal, QC, Canada

4.1 Abstract

4.1.1 Purpose

This study investigates the effectiveness of through-slice gradient optimization in dynamic slice-wise B_0 shimming to enhance signal recovery in cervico-thoracic spinal cord MRI, where thick axial gradient-echo images are often degraded by B_0 inhomogeneities, particularly at higher field strengths.

4.1.2 Theory and Methods

Six volunteers were scanned using a 15-channel AC/DC coil with dynamic shim updating (DSU) performed slice-by-slice. The optimization included a variable penalty parameter, w, to adjust the balance between in-plane B_0 homogeneity and through-slice gradient compensation. Acquisitions were compared using baseline shimming, DSU without through-slice compensation (w=0), and DSU with gradient compensation at values w=0.01, w=0.0001, and w=1.

4.1.3 Results

DSU with w=0.01 provided the best balance, significantly enhancing signal recovery and temporal signal-to-noise ratio (tSNR) at T2 (201%) and C3 (78%) vertebral levels compared to baseline. The higher penalty parameter w=1 was effective in simulations for reducing through-slice gradient-induced signal loss but led to instability and reduced image quality in actual acquisitions due to excessive in-plane B_0 inhomogeneities. Meanwhile, w=0 and w=0.0001 improved tSNR but failed to recover signal optimally in regions with large through-slice gradients.

4.1.4 Conclusion

Introducing a carefully balanced through-slice gradient parameter in slice-wise shimming, with w=0.01 as an optimal value, substantially improves signal recovery in axial gradient echo images of the spinal cord, without compromising in-plane homogeneity in a least squares sense. This efficient approach can advance spinal cord functional MRI applications at high field strengths.

4.1.5 Keywords

Spinal cord, Dynamic slice-wise B_0 shimming, AC/DC, multi-coil, Signal recovery, fMRI

4.2 Introduction

4.2.1 Challenges of Spinal Cord Imaging

Magnetic resonance imaging (MRI) of the spinal cord presents unique challenges due to its anatomical location, which limits efficient receive coil coverage, elongated size, and susceptibility-induced magnetic field distortions. The proximity of the spinal cord to air-tissue interfaces, such as the lungs, creates significant dynamic B_0 inhomogeneities that vary with respiration [14], [15]. Coupled with the spatially periodic B_0 variations caused by the bone-tissue interface of vertebral discs [7], [38], it is difficult to achieve accurate volume shimming. These inhomogeneities can lead to signal loss and image distortions in gradient-echo (GRE) EPI. Furthermore, the small cross-section size of the spinal cord requires high axial resolution [39], [42], which implies relatively thick slices (typically, 3-5 mm) to maintain an adequate signal-to-noise ratio (SNR). However, thick slices can introduce through-slice dephasing, resulting in signal loss in gradient echo imaging.

4.2.2 Advanced B_0 Shimming Solutions

Various approaches have been proposed to correct B_0 inhomogeneities in the spinal cord. One approach tailors the region of interest (ROI) to match the spinal cord's curvature, improving field homogeneity when combined with scanner spherical harmonics [43] or external shim-only coils [44]. This customization allows for more precise field correction than the scanner's rectangular shim box.

Dynamic slice-wise shimming [27] (DSU) refines this process by enabling slice-specific shim adjustments, often incorporating the customized ROI to optimize local shimming. This method has been effectively implemented in the spinal cord using scanner spherical harmonics [30], [45]–[47] and multi-coil systems [23]. Among these, integrated parallel reception, excitation, and shimming coils (iPRES [25], [33], [36]; AC/DC [31], [32]) represent specialized multi-coil designs that enhance DSU by providing highly localized field corrections. These approaches reduce distortions and improve signal recovery in the targeted region.

Real-time shimming builds on these methods by dynamically correcting for respiration-induced field variations. Monitoring the breathing cycle and adapting shim currents in real time mitigates time-varying distortions [23], [37], [48].

Despite their advantages, dynamic and real-time shimming techniques primarily focus on in-plane B_0 corrections and have limited impact on through-slice gradients, which remain challenging in thick-slice (GRE) spinal cord imaging. When shim optimization penalizes ΔB_0 in each voxel in a least-squares sense, it does not explicitly penalize the through-slice gradients.

4.2.3 Optimizing Through-slice Gradient for Signal Recovery

To address the issue of through-slice gradients in 2D spinal cord imaging, researchers have developed slice-specific z-shimming techniques, which involve applying tailored z-gradients across the slice to correct for dephasing [16], [40], [49], updated on a slice-by-slice basis. The process typically begins with acquiring EPI calibration scans where the z-gradient varies (e.g., 10 steps) across multiple volumes. These multiple acquisitions are then used to identify the z-gradient that provides the highest signal for each slice. One group extended to xyz-shimming [50], where the x, y, and z gradients are all optimized to enhance image quality further.

The slice-specific z-shimming technique offers several advantages, notably increasing signal and temporal signal-to-noise ratio (tSNR). Finsterbusch demonstrated that while a linear fit of the field effectively minimizes dephasing, it does not fully maximize signal recovery [51]. This method avoids this problem by optimizing signal intensity rather than addressing through-slice dephasing. Despite its advantages, the technique has some limitations. It does not account for the impact of gradients on in-plane B_0 homogeneity, which remains a key challenge for reducing geometric distortions. Additionally, this method can only address static field variations, as acquiring multiple EPI scans at different time points during the breathing cycle for each tested gradient would introduce significant time constraints. These time limitations also restrict slice-specific z-shimming to a low number of degrees of freedom (DOF). As seen with xyz-shimming, expanding the DOF increases calibration complexity and lengthens scan times. For example, a calibration scan for xyz-gradients took 5 minutes and 33 seconds to acquire 125 volumes for only five gradient values. This is a significant drawback in clinical applications where time efficiency is crucial.

Recent advancements in optimization algorithms have introduced a novel approach incorporating a through-slice gradient parameter into the mathematical mean squared error optimization process [35]. This innovative technique is synergistic with multi-coil systems, which

offer greater degrees of freedom than the scanner's linear gradients for high-spatial order B_0 shimming. Shim coils can also be employed for dynamic shim updating, enabling real-time adjustments to compensate for field variations. Since the optimization is field-based, this approach can effectively correct dynamic field inhomogeneities induced by breathing. While Willey *et al*. demonstrated the potential of this method in the brain [35], it is anticipated that it could be even more beneficial for the spinal cord, where through-slice dephasing is very prevalent due to the use of thick axial slices and the presence of strong B_0 inhomogeneities in GRE-EPIs, especially in the lower cervical and thoracic cord.

The current study focuses on the following objectives:

1. **Implement dynamic slice updating:** Integrate dynamic slice-specific shimming to make the experience viable for fMRI and clinical applications.
2. **Develop a fully automated pipeline:** Implement an automated workflow for shimming using an AC/DC coil and the signal recovery optimizer. Incorporate these new algorithms into *Shimming Toolbox* [52] for broader accessibility and use.
3. **Assess the trade-off between signal recovery and geometric distortions:** Evaluate the impact of signal recovery optimization with an AC/DC coil on signal intensity and geometric distortions in GRE-EPIs of the cervical and upper thoracic spinal cord.

4.3 Methods

4.3.1 Theory

In this section, we describe the algorithm used to compute the shimming coefficients, along with the regularization term designed to account for through-slice dephasing. The signal recovery implementation in this work is based on a mean squared error (MSE) optimization.

The optimization function for MSE is defined in Eq. 4.1:

$$min_I \ \frac{1}{N}\sum_{a=1}^{N}\left(\Delta B_{0,shimmed}(I)\right)^2 \tag{4.1}$$

Where $\Delta B_{0,shimmed}$ represents the shimmed field as defined below.

$$\Delta B_{0,shimmed}(I) = \Delta B_{0,baseline} + \sum_{c=1}^{n} I_c \cdot \Delta B_{0,c} \tag{4.2}$$

Where $\Delta B_{0,baseline}$ is the baseline field, $\Delta B_{0,c}$ is the coil profile of channel c, N is the number of voxels, I_c is the current in channel c, and n is the number of channels in the coil.

In most implementations of dynamic shimming, where this optimization is applied slice by slice, the through-slice gradient is not explicitly compensated. Although some optimization methods account for the adjacent slices [20], [22], [24], [52], [53] (or an additional slice in the through-slice direction [30]) when performing slice-wise shimming, adjacent slices are not a good surrogate of the actual dephasing that occurs within the slice in question.

To address this issue, Willey et al.[35] modelled the signal loss L explicitly as shown in Eq. 4.3, assuming a rectangular slice profile, uniform spin density across the slice, and a linear field variation through the slice:

$$L = 1 - \left|sinc\left(\frac{\phi}{2}\right)\right|, \tag{4.3}$$

where Φ is the phase dispersion:

$$\phi = \gamma \frac{\partial B_0}{\partial z} \Delta z \cdot TE \tag{4.4}$$

Where γ is the gyromagnetic ratio, $\frac{\partial B_0}{\partial z}$ the through-slice gradient, Δz is the slice thickness and TE is the echo time.

In Eqs. 4.3 and 4.4, the through-slice gradient is the only parameter that can be adjusted through shimming. Therefore, Eq. 4.1 was modified to incorporate signal recovery optimization, as shown in Eq. 4.5:

$$min_I \ \frac{1}{N}\sum_{a=1}^{N}\left(\left(\Delta B_{0,shimmed}(I)\right)^2 + \ w\left(\frac{\partial B_{0,shimmed}(I)}{\partial z}\right)^2\right) \quad 4.5$$

Where *w* is a weighting parameter that balances the signal recovery objective with the standard MSE optimization.

4.3.2 Participants

Six healthy volunteers (3 males, 3 females; mean age 24.3, standard deviation 0.47) underwent MRI scans on a Siemens 3T Prisma-fit scanner. All procedures were approved by an institutional review board (IRB) and followed ethical guidelines. Participants were selected to ensure a balanced representation of both sexes, with no specific criteria for age or health status.

4.3.3 Experiment

Participants were scanned using a custom-built 15-channel AC/DC coil [32] displayed in Figure 4.1. In the AC/DC approach, B_0 shim capability is introduced into the loops of an RF receive array by using high-impedance chokes to create a DC path through the loop [31]. The coil's DC component was driven by open-source shim amplifiers [24]. Currents were restricted to 2.5 A per channel and 25 A for all 15 channels.

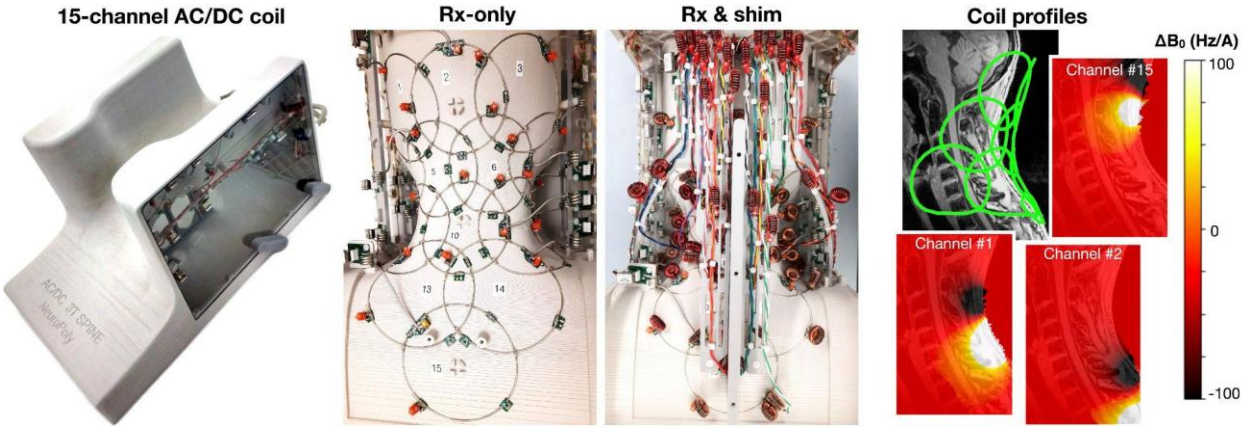

Figure 4.1 Bottom view of the 15-channel AC/DC coil before (receive array – Rx-only) and after (AC/DC – Rx & shims) adding the shimming capabilities. The AC/DC coil loops' positions are superposed on the T1w image with an example for three different channels' generated fields (coil profiles).

4.3.3.1 Baseline Acquisition

After the localizer, a shim box is automatically fitted to the region of interest, and an adjustment volume is performed with the scanner's 0-2nd order spherical harmonic shims.

Employing this new shim, a baseline GRE-EPI (axial, 1x1x5mm, TE=32ms, TR=2070ms, FA=70°, Partial Fourier=⅞, lipid saturation, 10 volumes) was acquired in both AP and PA phase encoding directions to assess geometric distortions induced by the B_0 field. A PA sequence with 60 volumes was also collected to calculate the tSNR.

An MPRAGE (1x1x1mm, TE=3.72ms, TR=2000ms, FA=9°) scan was obtained for segmentation and visualization. Finally, two GRE B_0 field maps were acquired. The first field map, used for the optimization (axial, 2.8x2.8x2mm, TE=[2.68ms, 4.92ms], TR=705ms, FA=65°), comprised 100 slices to achieve enhanced resolution in the slice direction. The second field map

(axial, 1.4x1.4x5mm, TE=[2.68ms, 4.92ms], TR=20ms, FA=13°) was acquired to match the slice coverage of the EPIs, enabling subsequent acquisition of the shimmed field.

The additional steps needed for shimming take approximately 16 minutes: 10 minutes to set up, 3min28 for the MPRAGE, 45 seconds for the field map and 2 minutes for the segmentation and optimization. This time could be shortened using the localizer as the segmented image instead of the MPRAGE. Also, if the scanner room provides an AC/DC coil with the shimming setup already preinstalled, the setup time of 10 minutes could be saved.

4.3.3.2 Optimization

Figure 4.2 illustrates the optimization pipeline described below. Please refer to the GitHub repository for the complete optimization scripts.

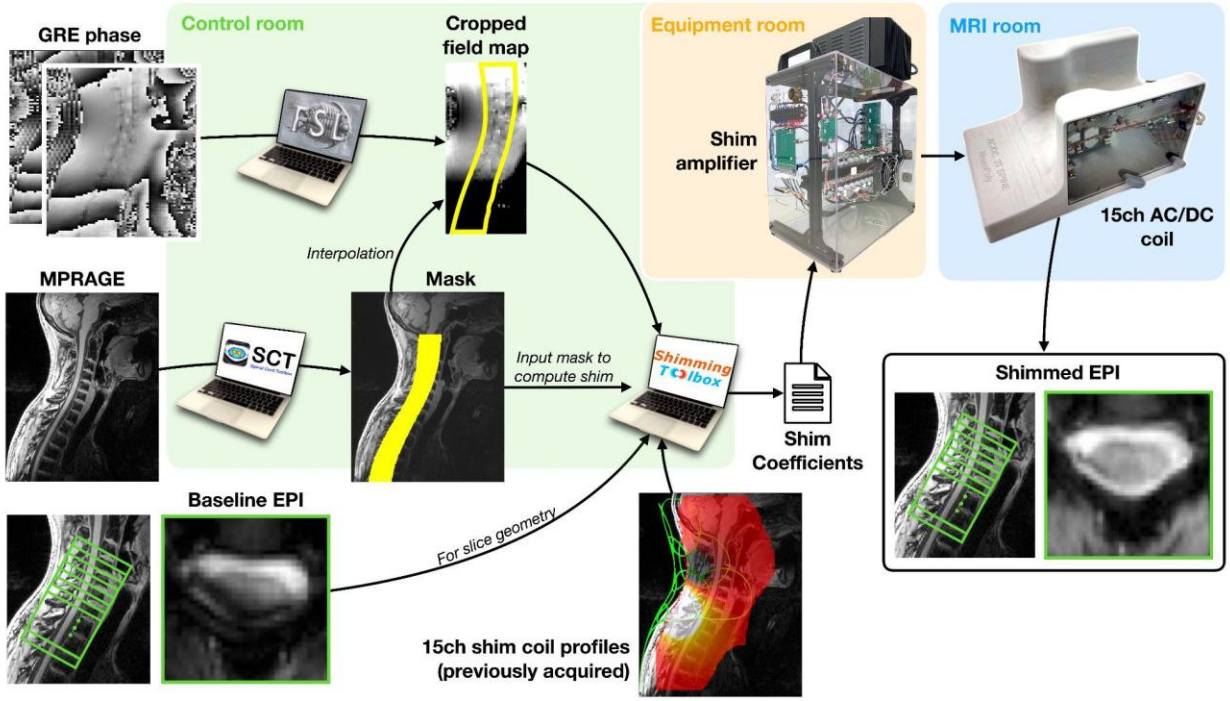

Figure 4.2 Pipeline of the experiments. GRE phases from the field mapping sequence are passed along with the mask generated by SCT [54] to the Shimming Toolbox [52] (FSL's prelude [57]) which returns a field map cropped to fit the mask. The field map, the mask, the EPI and the coil profiles for the 15-channel AC/DC coil are passed to *Shimming Toolbox* which returns the shimming coefficient for the required optimization. The coefficients are then set on the shim amplifiers which control the coil's currents during the experiment to acquire a shimmed EPI.

The Baseline acquisition DICOM files were sorted and converted to NIfTI format using *Shimming Toolbox*. Subsequently, the spinal cord on the MPRAGE was segmented using *Spinal Cord Toolbox* [54] (SCT v6.3) with the sct_deepseg command [55] and the contrast agnostic model [56]. With this segmentation and SCT, two cylindrical masks were generated centred on the spinal cord. The field map mask had a diameter of 40 mm, while the optimization mask had a diameter of 25 mm. The field map mask was larger to ensure accurate resampling due to the differing orientations of the MPRAGE and EPI slices.

Next, the field map was computed using *Shimming Toolbox* (with FSL [57]) and the 100-slice GRE acquisition. Using this field map, the 15-channel AC/DC coil currents were optimized

for each EPI slice and two signal loss parameters: 0 (regular slice-wise shim, no consideration for the through-slice gradient) and 0.01. The optimization was conducted to minimize the mean squared error of the B_0 field using a least-squared optimizer. One of the six subjects was evaluated with two additional optimization parameters (0.0001 and 1) to assess the impact of the signal loss parameter. The value of 0.01 was based on simulations with various parameter values on field maps acquired before the first experiment. The Python tool *scipy.optimize.minimize()* [58] was used to solve the least square equation to find optimal shim currents subject to current constraints.

4.3.3.3 Shimming Acquisitions

Each optimization acquisition followed a standardized procedure. Initially, the optimized currents were uploaded to the shim amplifiers. Subsequently, all baseline EPIs (AP, PA, tSNR) were reacquired. The EPI pulse sequence was modified to generate a transistor-transistor logic (TTL) trigger before each RF pulse. The shim amplifiers captured these triggers and adjusted the AC/DC coil currents for the subsequent slice.

Since the field optimization was confined to a small mask, the field outside could interfere with fat saturation. To avoid this issue, an additional TTL trigger was inserted before every fat saturation pulse to zero out the currents. Following the EPI acquisitions, the baseline B_0 field map with the same slices as the EPIs was acquired. The GRE sequence mapping of the B_0 field was also modified to send a TTL trigger before each new slice.

4.4 Results

Figure 4.3 illustrates the trade-off between signal loss and B_0 slice homogeneity. An MPRAGE image of the same slice imaged by the EPI serves as a reference, depicting the spinal cord's geometry without signal loss or geometric distortions. The figure demonstrates a sharp and consistent decrease in B_0 RMSE when using dynamic shim updating (DSU) with a signal penalty parameter (w) of 0.01 or lower. In contrast, a higher value (w = 1) results in a B_0 field RMSE similar to the baseline. This is evident in the EPI images, where the spinal cord in the final column (w = 1) appears distorted in the posterior direction due to B_0 inhomogeneities.

Regarding signal loss, even the DSU that doesn't account for signal recovery (w = 0) shows improvement in the signal loss map, as the optimizer includes contributions from the slice above and below the target slice. However, the signal loss significantly decreases with w = 0.01 and 1, resulting in much higher signal quality in the EPI images. Notably, there is a clear correspondence between the signal loss maps and the EPIs. For instance, the w = 0.01 signal loss map shows a drop in signal at the top of the region of interest (ROI), which is also reflected in the corresponding EPI image.

It is important to note that with a signal loss penalty (w) of 1, the required shimming currents were substantially higher (approximately 15 amps per slice, compared to less than 5 amps for other optimizations), and the image quality across slices was inconsistent. Additionally, as shown in Figure 4.6, the more inferior slices (T3 level) typically do not exhibit significant signal improvement in the EPIs.

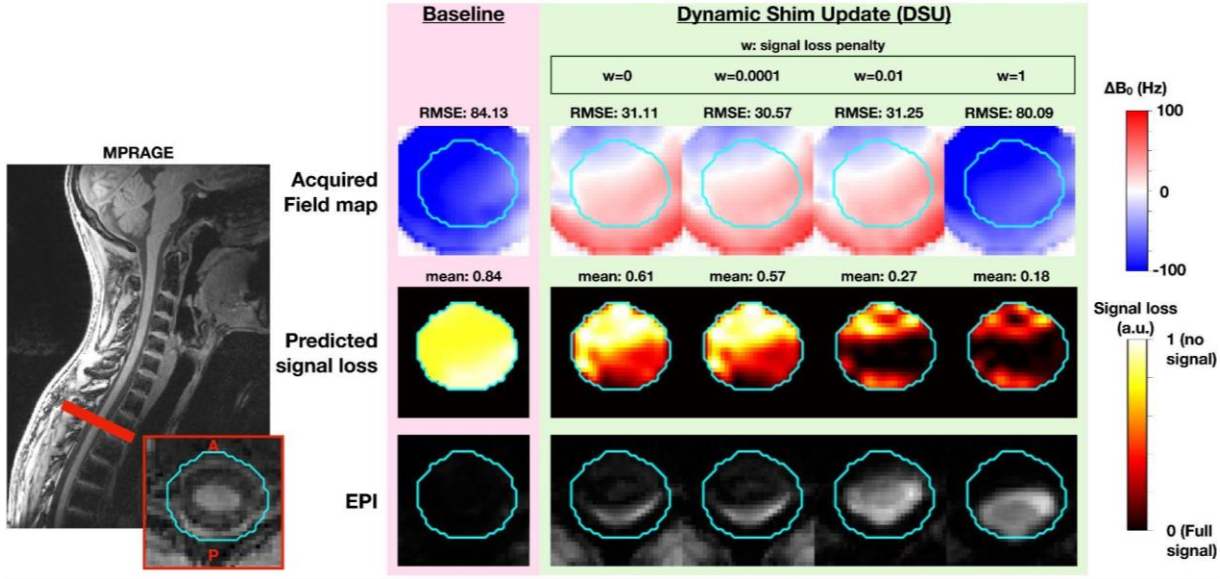

Figure 4.3 MPRAGE, acquired field map, predicted signal loss maps and EPIs for one slice of the same subject for the baseline and for different signal loss penalty parameters (w = [0, 0.0001, 0.01, 1]) from Eq. 4.5. The signal loss maps were computed using Eq. 4.3. The light blue trait is the contour of the ROI used for the shimming optimization. The contour was initially in the MPRAGE reference frame and was resampled in the EPI's reference frame. All optimizations apart from baseline were dynamically shim updated (DSU) with the 15-channel coil's channels.

Figure 4.4 presents all 25 slices for subject 6 across three acquisitions: baseline (scanner shim), dynamic shim update (DSU) with no signal loss penalty (optimizing only for in-plane B_0 homogeneity), and DSU with a 0.01 signal loss penalty (optimizing for both in-plane B_0 homogeneity and through-slice gradient). Image quality in the baseline acquisition is notably worse in the C3 and C4 slices. From C5 to C7, the baseline offers comparable geometric distortions and signal drop-offs to the other two shimmed acquisitions. Below T1, a clear signal drop-off is observed in the baseline acquisition compared to the DSU conditions. The DSU without signal recovery optimization (w=0) begins to diverge from the DSU with signal recovery (w=0.01) at T2 and no acquisitions provide a visible spinal cord at T3 level.

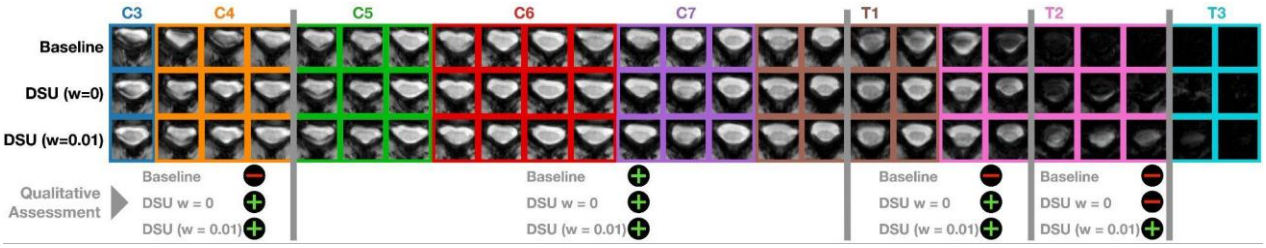

Figure 4.4 25 axial slices covering C3 to T3 vertebral levels, cropped around the spinal cord, for 3 scenarios: baseline, dynamic shim updating (DSU) without signal loss penalty (w=0) and DSU with signal loss penalty (w=0.01). All optimizations apart from baseline were dynamically shim updated (DSU) with the 15-channel coil's channels. The image scaling is the same across the three scenarios.

Figure 4.5 presents two EPI slices from the same subject, for AP and PA phase encoding directions. As the signal loss penalty (w) increases, the distortions become more pronounced. This is expected, as higher *w* values shift the optimization's focus towards minimizing the through-slice gradient at the expense of in-plane B_0 homogeneity, thereby exacerbating geometric distortions. The baseline acquisition shows even greater geometric distortions in slices where the initial B_0 homogeneities were poorly corrected by the scanner's 0-2nd order spherical harmonic shim. The blue slice exhibits geometric distortions that are more pronounced than the orange slice, despite the latter being in a typically more challenging environment due to its proximity to the lungs. This artifact will be further discussed in the next section.

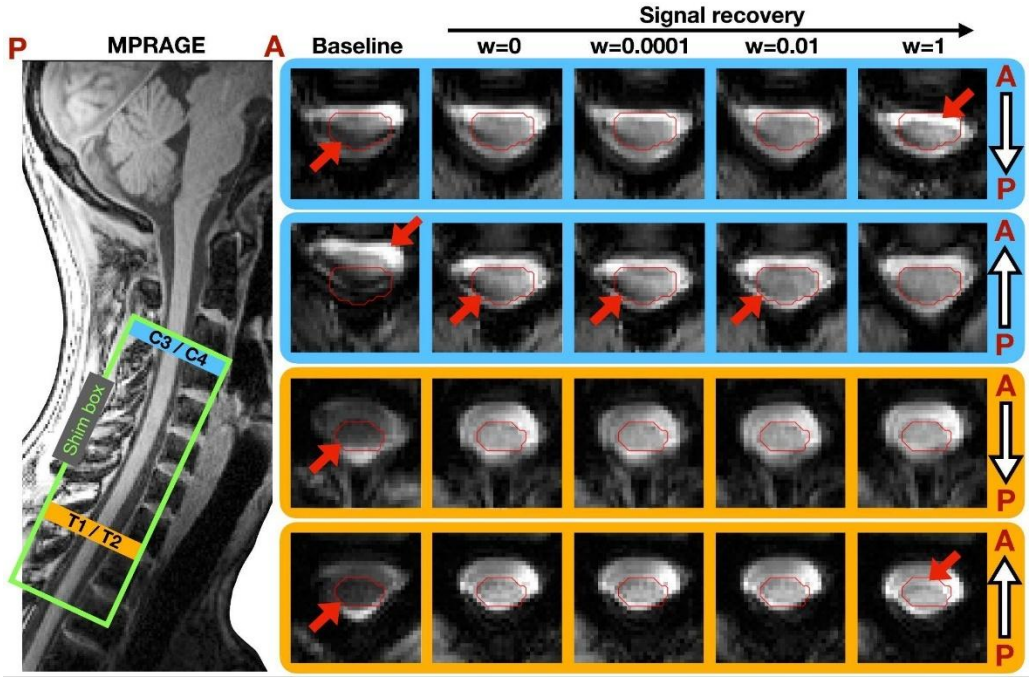

Figure 4.5 EPI images for two slices were acquired in AP and PA phase encoding directions. The anatomical locations of the shown slices are indicated on the MPRAGE. The red spinal cord contour is based on the MPRAGE image and has been resampled in the EPI space. All optimizations apart from baseline were dynamically shim updated (DSU) with the 15-channel coil's channels.

Figure 4.7 and Figure 4.6 illustrate the effect of the signal loss penalty on predicted signal loss across different vertebral levels and its correlation with the acquired tSNR and tSNR improvements from the baseline acquisition. Predicted signal loss was computed with *Shimming Toolbox* using Eq. 4.3, mean tSNR was calculated from the 60 EPI volumes using the code available on GitHub and tSNR improvement is the average improvement in each vertebral level for each subject. Signal loss is most pronounced at the T2 and T3 vertebral levels, while it is minimal from C4 to T1, with a slight increase at the edge of the volume of interest in C3. The tSNR follows a similar pattern to the signal loss.

For different shimming methods, a clear correlation emerges between the predicted signal loss and the acquired tSNR from C3 to T1. However, at T2 and T3, while DSU with a signal penalty parameter of $w = 0.01$ yields better tSNR, the improvement does not fully reflect the predicted signal recovery. With a higher parameter ($w = 1$), the lower slices proved even more challenging to shim than expected, resulting in an overall tSNR lower than that achieved with the lower signal recovery parameter ($w = 0.01$).

Overall, the greatest signal improvements from signal recovery optimization are observed at T2, where the initial signal loss was substantial, with a 201% average improvement, and in C3, where a notable drop-off in signal was observed in the baseline acquisition, with a 78% average improvement.

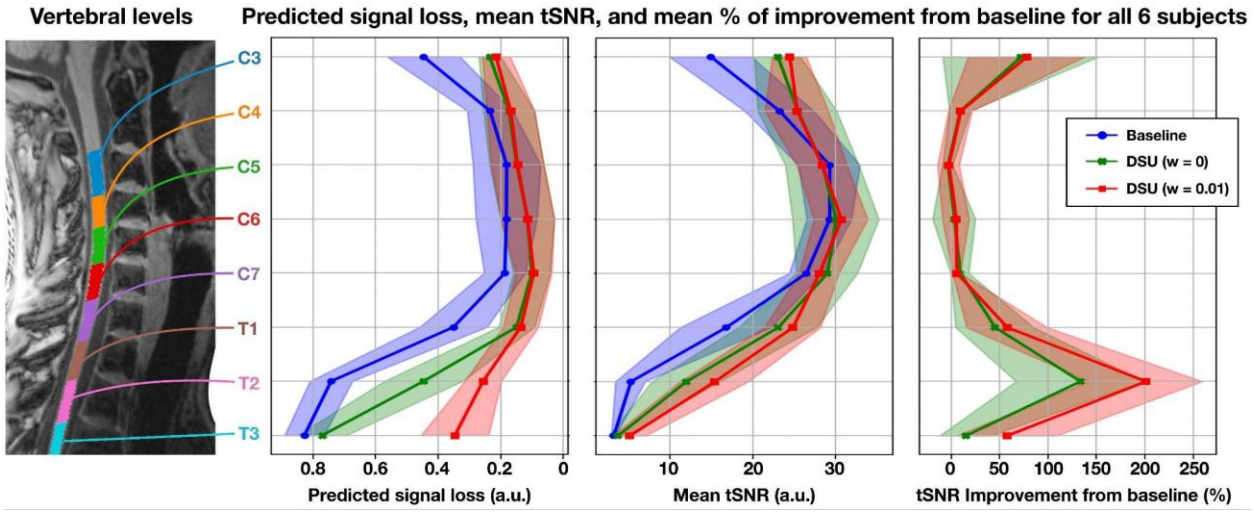

Figure 4.7 Predicted signal loss, mean tSNR and tSNR improvement from baseline for all 6 subjects with a 95% confidence interval computed using bootstrapping. Each of the 25 slices was distributed to vertebral levels using SCT's segmentation shown on the left. The values on the plots represent the average of every slice attributed to the vertebral level. Improvement from baseline represents the individual improvement from each subject relative to their baseline acquisition. All optimizations apart from baseline were dynamically shim updated (DSU) with the 15-channel coil's channels.

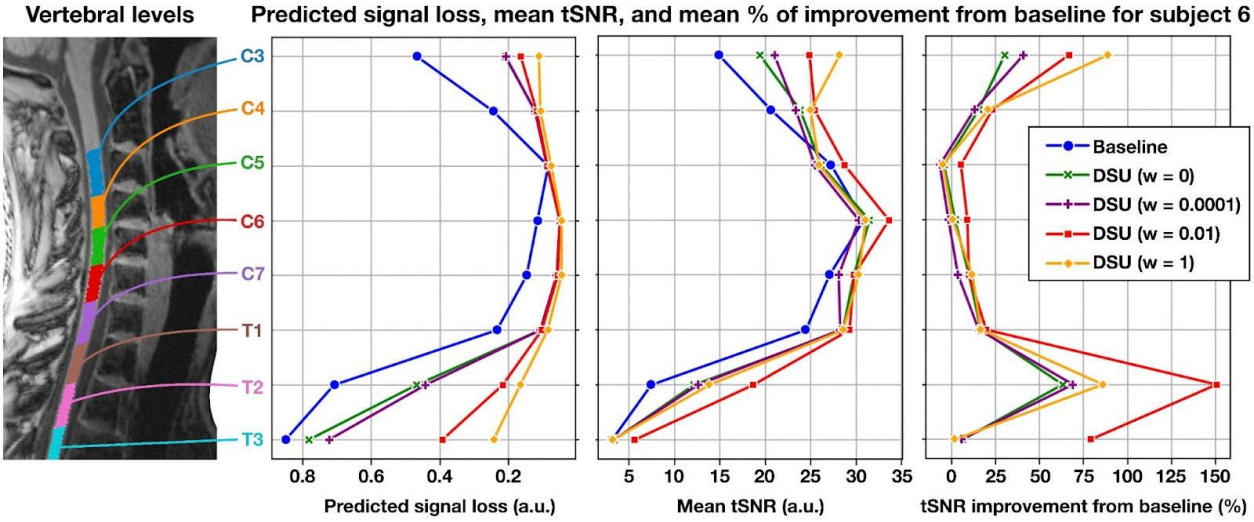

Figure 4.6 Predicted signal loss, mean tSNR and tSNR improvement from baseline for subject 6 as the optimization parameter is varied (Baseline, w = [0, 0.0001, 0.01, 1]). Each of the 25 slices was distributed to vertebral levels using SCT's segmentation on the left. The values on the plots represent the average of every slice attributed to the vertebral level. All optimizations apart from baseline were dynamically shim updated (DSU) with the 15-channel coil's channels.

Figure 4.8 and Figure 4.9 display the in-plane B_0 RMSE distribution across all axial slices. Figure 4.8 is all six subjects and Figure 4.9 is subject 6 only, who was tested with two additional *w* parameters. Dynamic shim updating led to a mean reduction in RMSE over all 6 subjects of 71% when optimizing only for in-plane B_0 homogeneity ($w = 0$) and a 66% reduction when jointly optimizing in-plane B_0 homogeneity and the through-slice gradient ($w = 0.01$). The higher RMSE values, particularly noticeable in subjects 2 and 4 during signal recovery optimization ($w = 0.01$), are due to lower slices in T3, where signal loss is severe and the spine is not visible in the EPIs, even after shimming. This causes the optimizer to overcompensate for the through-slice gradient, leading to a higher in-plane B_0 RMSE. When comparing the different optimizations' axial B_0 RMSE with the baseline using a Mann-Whitney U test, both showed a significant difference (w=0: p_{val} = 3.3e-04 < 0.05; w=1: p_{val} = 4.9e-03 < 0.05). No difference was found when comparing them to each other (p_{val} = 0.187 > 0.05). In Figure 4.9, for subject 6, B_0 RMSE is similar across $w = 0$, $w = 0.0001$, and $w = 0.01$. However, at the other extreme, using $w = 1$ results in a worse overall RMSE than the baseline acquisition.

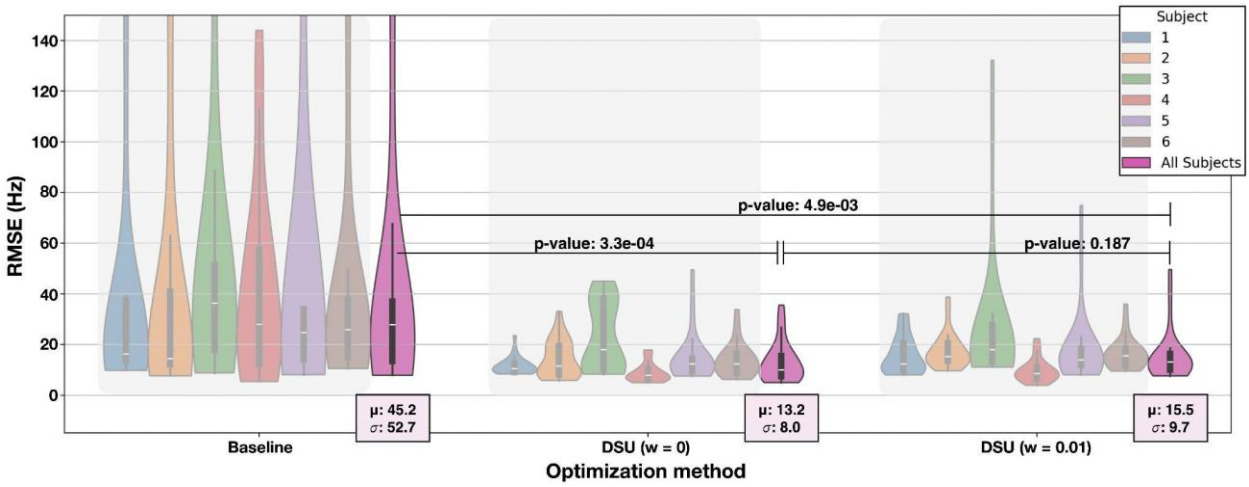

Figure 4.8 Violin plots of the mean in-plane B_0 RMSE for every slice of every shim for all 6 subjects. The dynamic shim updates (DSU) are optimized with different *w* values from Eq. 4.5. The mean and standard deviation of the distribution were computed for each optimization of each subject. P-values were calculated using the Mann-Whitney U test comparing the combination of all subjects into a single distribution (all subjects). All optimizations apart from baseline were dynamically shim updated (DSU) with the 15-channel coil's channels.

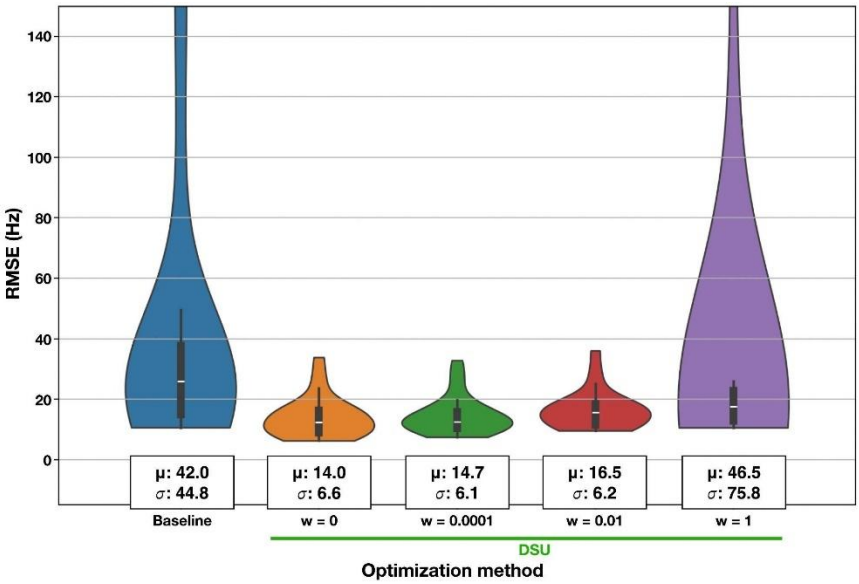

Figure 4.9 Violin plots of the mean in-plane B_0 RMSE for every slice for subject 6. The mean and standard deviation of the distribution were computed for each optimization. As the signal loss penalty (w) from Eq. 4.5 increases, the optimization favours signal recovery over in-plane B_0 homogeneity. All optimizations apart from baseline were dynamically shim updated (DSU) with the 15-channel coil's channels.

4.5 Discussion

4.5.1 Optimization Evaluation

This study evaluated the signal recovery optimization outlined in Eq. 4.5 by comparing its performance in the cervicothoracic spine (C3 to T3) to the scanner's baseline shim and the conventional B_0 optimization described in Eq. 4.1. The baseline shim optimized the entire volume of interest (VOI), while the two other methods applied dynamic updates for each acquired slice.

Signal recovery optimization ($w = 0.01$) proved highly effective in the upper thoracic region (Figure 4.4Figure 4.6, and Figure 4.7), with tSNR improvements over baseline of 58%, 201%, and 58% for T1, T2 and T3 vertebral levels respectively. Standard B_0 optimization ($w = 0$) also showed tSNR gains in these regions: 46% at T1, 134% at T2, and 16% at T3. While the T1 vertebral level exhibited similar tSNR improvements in both slice-wise optimizations, the greater predicted signal loss in T2 and T3 made through-slice gradient minimization ($w = 0.01$) particularly beneficial.

In the C3 region, baseline EPI acquisitions showed inconsistency and increased signal loss. Both dynamic slice-wise shimming methods ($w = 0$ and $w = 0.01$) resolved this issue, leading to average tSNR increases of 72% ($w = 0$) and 78% ($w = 0.01$). These results are corroborated by the EPI images for subject 6 in Figure 4.4, where slice-wise shimming improves image quality in C3 and T1, with the signal loss penalty ($w = 0.01$) further enhancing the image in the T2 vertebral level. However, no shimming optimization achieved sufficient image quality in the T3 region, likely due to the highly temporally varying B_0 field in this region due to breathing in combination with a relatively low RF receive coil sensitivity causing an unreliable B_0 field map.

As the signal loss penalty involves balancing the through-slice gradient and in-plane B_0 homogeneity, B_0 RMSE was analyzed to assess the performance drop-off due to the trade-off. Optimizing only for in-plane B_0 homogeneity ($w = 0$) led to a B_0 RMSE reduction of 71% while incorporating the through-slice gradient in the optimization ($w = 0.01$) achieved a 66% reduction. This 5% difference was statistically non-significant, as confirmed by a Mann-Whitney U test ($p = 0.187 > 0.05$). Introducing a signal loss penalty of 0.01 effectively enhanced signal recovery, particularly in a low T2 slice with substantial signal loss, without compromising B_0 homogeneity compared to standard in-plane optimization. This is clearly illustrated in Figure 4.3, where the penalty greatly improves the signal while maintaining similar in-plane B_0 characteristics.

The slice at the edge of the shimmed volume (blue slice in Figure 4.5) exhibited substantial geometric distortions compared to a slice located further down in the thoracic region (orange slice), which is counterintuitive as we expect more B_0 field inhomogeneity in the upper thoracic cord compared to the upper cervical cord as shown in previous studies. We think this unexpected result is related to how the vendor's volume shim operates: optimal shim coefficients are calculated based on voxels inside the green box shown in Figure 4.5, but given the relatively spatially smooth variation of the field, voxels inside the ROI have more contribution than those at the edge of the ROI (such as those of the blue slice) because those at the edge don't benefit from the contribution from neighbouring voxels outside the ROI. The volume shim was a critical starting point in our experiment since the slice-wise shimming only relied on the external AC/DC coil. In future studies, the scanner gradients and the external AC/DC coils should be optimized jointly for slice-wise shimming, hopefully addressing this issue.

4.5.2 Signal Loss Penalty Evaluation

The effect of the signal loss penalty was further investigated in one of the six subjects by repeating the acquisitions for two additional w parameters: 0.0001 and 1. A small penalty (w = 0.0001) produced results similar to regular B_0 optimization (w = 0) in both in-plane B_0 RMSE and signal loss, suggesting that such a small penalty does not offer any noticeable improvements.

At the other extreme, using a large weight of 1 for through-slice gradient optimization showed only marginal improvements in predicted signal loss compared to a penalty of 0.01, while significantly increasing B_0 RMSE. This optimization resulted in an overall field worse than the baseline acquisition, as illustrated in Figure 4.9. Moreover, the improved predicted signal loss did not correspond to better tSNR in the lower part of the field of view (FOV) (Figure 4.7). One likely explanation is that the required coil currents were three times higher on average. Higher currents often lead to more unstable acquisitions and less reliable results, as any errors in the generated field scale proportionally with the current. Additionally, since the coil currents are set to zero during the fat saturation pulse that precedes each slice acquisition, the larger current transitions might induce eddy currents. These steeper transitions could also cause current instability at the start of each acquisition, leading to an unstable field.

Another reason why the higher signal loss penalty (w = 1) did not yield better tSNR than the lower penalty (w = 0.01) was that the predicted signal loss improvements were marginal and not concentrated in the spinal region where tSNR is measured. The shimming mask used was slightly larger than the spinal cord (25 mm diameter), meaning improvements may have occurred outside the region of interest.

Ultimately, a signal loss penalty of 0.01 proved optimal, striking the best balance between minimizing geometric distortions and maximizing signal recovery.

4.5.3 Plans and Improvements

An intriguing finding observed in some subjects was that signal recovery optimization occasionally resulted in worse signal loss in small specific regions of the spine, even though the overall signal loss within the ROI was lower than traditional B_0 optimization. This issue arises because the binary mask used for the ROI is larger than the spinal cord itself, leading to a focus on overall signal loss without consideration for where the loss occurs within the mask. A soft mask could address this while maintaining a more flexible ROI that includes a small region outside the spinal cord (to avoid distortions near the spine). This soft mask would assign a value of 1 to voxels within the spinal cord and gradually reduce the value from 1 to 0 using a Gaussian curve for voxels outside the cord.

To further improve image quality, future signal recovery optimization could account for the subject's breathing cycle, which induces field variations as described in previous studies[14], [15]. Breathing causes a B_0 offset and generates a through-slice gradient, as the f_0 offset varies depending on the location along the spine. Incorporating this into the signal recovery optimization could help mitigate breathing-induced through-slice gradients.

Another limitation of this study was the shim coil design. Our AC/DC coil was optimized for the cervical spine, with a higher density of receive and shim loops in that region, but it only features one loop near the T2 and T3 vertebral levels, limiting the degrees of freedom for shimming in this area. This limitation is especially problematic when current in the more distant loops is restricted. Designing a new coil optimized for the thoracic spine could be crucial for further improving GRE-EPI images in this region.

This study focused exclusively on the through-slice gradient due to the high in-plane resolution relative to the slice thickness (1x1x5 mm). However, in studies that experience signal loss at different resolutions, in-plane gradients could also be incorporated into the optimization. This capability is already available in the *Shimming Toolbox.*

Finally, since the optimization is efficient and requires only an additional EPI scan (25 seconds) and a field map (45 seconds), this shimming method has the potential to enhance BOLD fMRI research in the cervicothoracic spine by improving image quality and reducing signal loss.

4.6 Conclusions

In this study, we evaluated the effectiveness of dynamic slice-wise shimming and signal recovery optimization in reducing signal loss and improving image quality in the cervicothoracic spine. Results demonstrated that incorporating a signal loss penalty ($w = 0.01$) provided the optimal balance between minimizing geometric distortions and enhancing signal recovery, particularly in the upper thoracic region, where through-slice gradient minimization proved essential. Although limitations in coil design affected performance at the thoracic levels, future improvements, such as using a soft mask and accounting for breathing-induced field variations, could further enhance the technique's potential. Given its quick and efficient optimization process, this method holds promise for improving BOLD fMRI studies and 2D gradient echo anatomic images in the spine.

4.7 Acknowledgments

Funded by the Canada Research Chair in Quantitative Magnetic Resonance Imaging [CRC-2020-00179], the Canadian Institute of Health Research [PJT-190258], the Canada Foundation for Innovation [32454, 34824], the Fonds de Recherche du Québec - Santé [322736, 324636], the Fonds de Recherche du Québec - Nature et technologies [329439], the Natural Sciences and Engineering Research Council of Canada [RGPIN-2019-07244], the Canada First Research Excellence Fund (IVADO and TransMedTech), the Courtois NeuroMod project, the Quebec BioImaging Network [5886, 35450], INSPIRED (Spinal Research, UK; Wings for Life, Austria; Craig H. Neilsen Foundation, USA), Mila - Tech Transfer Funding Program, and the NIH NIBIB R01 EB028797, P41 EB030006, and U24 EB028984.

4.8 Supporting Information

- All scripts used for this paper are available on this GitHub repository: https://github.com/4rnaudB/spinalcord-signal-recovery/releases/tag/v1.0
- All data acquired for this paper is available on OSF at this link: https://osf.io/rs6tv/
- The design files for the 15-channel AC/DC coil are available at this link (DOI: https://doi.org/10.5281/zenodo.14271010)

CHAPTER 5 Discussion

5.1 Shimming Operating System & Coil Implementation

The initial four months of the master's program focused on conducting a literature review and implementing the shimming system [41]. Upon arrival in the lab, the shim system faced persistent breakdowns, had only 8 functional channels, and was unable to receive TTL triggers at the necessary speed.

To repair the shim board presented in Figure 5.1, it was necessary to learn PCB schematic interpretation and effectively use a multimeter and function generator. These tools identified and resolved multiple soldering issues through surface-mount soldering techniques.

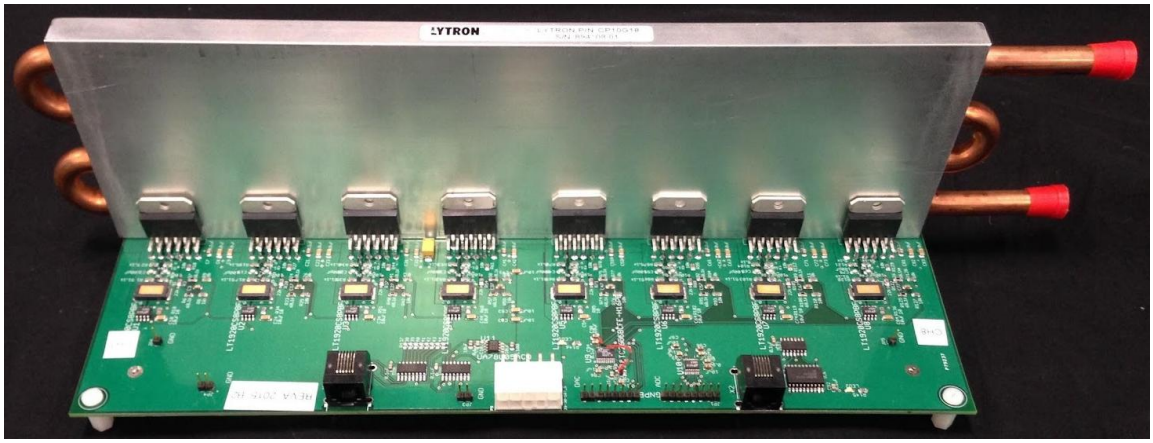

Figure 5.1 8-channel shim board picture with heatsink

After repairing the initial 8 channels, functionality was tested and validated using a prototype 8-channel coil. With the system successfully validated, a second shim board was populated, expanding the setup to 16 channels in total.

The final issue to address involved the TTL trigger input. Initial tests revealed that the system failed to count the expected number of TTL triggers. Sequence validation indicated that TTL triggers, received via BNC cable, passed through a secondary circuit that stretched each trigger to 10 ms—exceeding the gap between triggers in the sequence. Consultation with the MR specialist at the UNF confirmed that the trigger could instead be acquired as a fibre optic input before this stretching occurred, allowing the system to count each trigger accurately.

Finally, some small modifications had to be done on the new 15-channel coil before shimming was possible.

5.2 Development of the GUI Control Interface

The shim system was designed for flexible deployment across a range of shimming experiments, necessitating an adaptable and user-friendly setup that allowed rapid modifications to minimize subject time in the scanner. To support this flexibility, the Teensy's code was not only restructured for modularity—enabling future integration of new shimming methods—but also programmed to run the experiments currently required for the system. Additionally, serial communication functionality was implemented to enable seamless interaction with a host computer. For more efficient and reliable data transfer, the initial RS-232 cable was replaced with a 20-meter USB cable with repeaters, necessitating minor circuit modifications to the Teensy to accommodate USB compatibility.

To facilitate user interaction, a custom Python-based interface (Figure 5.2) was developed to communicate with the Teensy during experimental procedures. This interface is available in the organization's GitHub repository (https://github.com/shimming-toolbox/Teensy-communication) and is organized into two primary sections: Commands and Experiments.

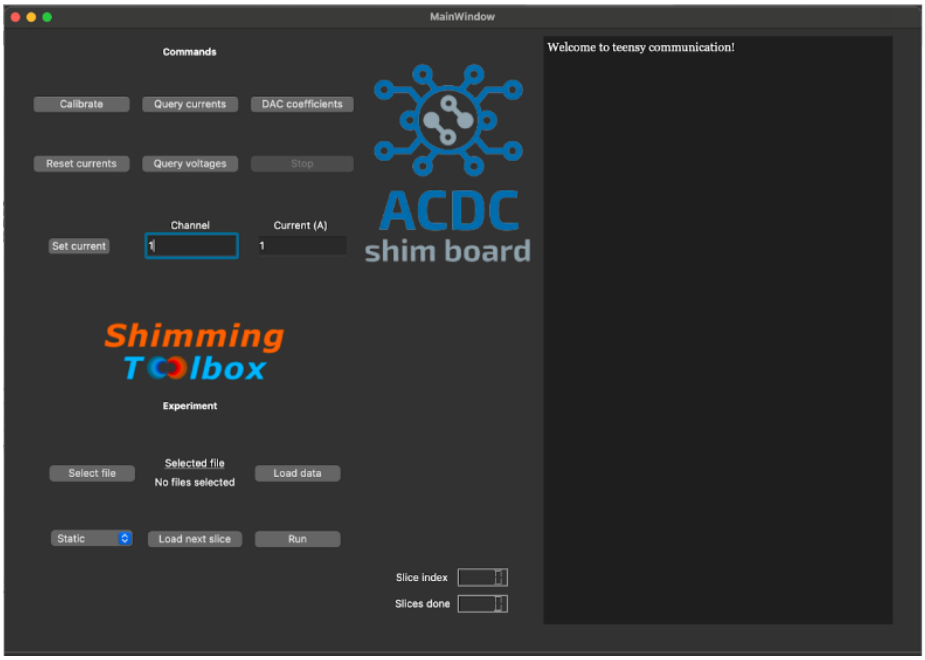

Figure 5.2 Python GUI for teensy communication

The Commands section includes functionalities for calibrating the shimming system's digital-to-analog converter (DAC) values, which is necessary before each experiment to ensure accurate current readings in each loop. Additionally, this section enables the user to query current, voltage, and DAC coefficients across all channels, allowing real-time system diagnostics and ensuring optimal performance of the shimming hardware. It also includes features to set specific current values to individual channels, reset all channels to zero, and terminate ongoing experiments.

The Experiments section enables users to select and initiate specific shimming experiments, currently offering options for volume shimming and dynamic slice-wise shimming (see sections 2.3.3.1 and 2.3.3.2). Before running an experiment, the shim coefficients are uploaded to the Teensy by importing a Shimming Toolbox-formatted text file, facilitating a seamless workflow from Shimming Toolbox optimizations to in-experiment shimming. This setup ensures that the shimming process is both efficient and adaptable to the specific requirements of each experimental protocol.

5.3 Dynamic Slice-wise Shimming in the Spinal Cord

Once the shimming system was operational, the first experiments focused on dynamic slice-wise shimming of the cervicothoracic spinal cord using a 15-channel AC/DC coil. Previously, only one other group at Duke University had conducted similar experiments [33], though without achieving dynamic slice updating (DSU). Implementing DSU required modifications to the IDEA sequence code to add TTL triggers before each slice and fat saturation pulse in both GRE-EPI and GRE field map sequences. Following successful implementation, three subjects were scanned using this fully automated and open-source pipeline. This work culminated in an ISMRM conference abstract [32], with the primary findings presented in Figure 5.3 below.

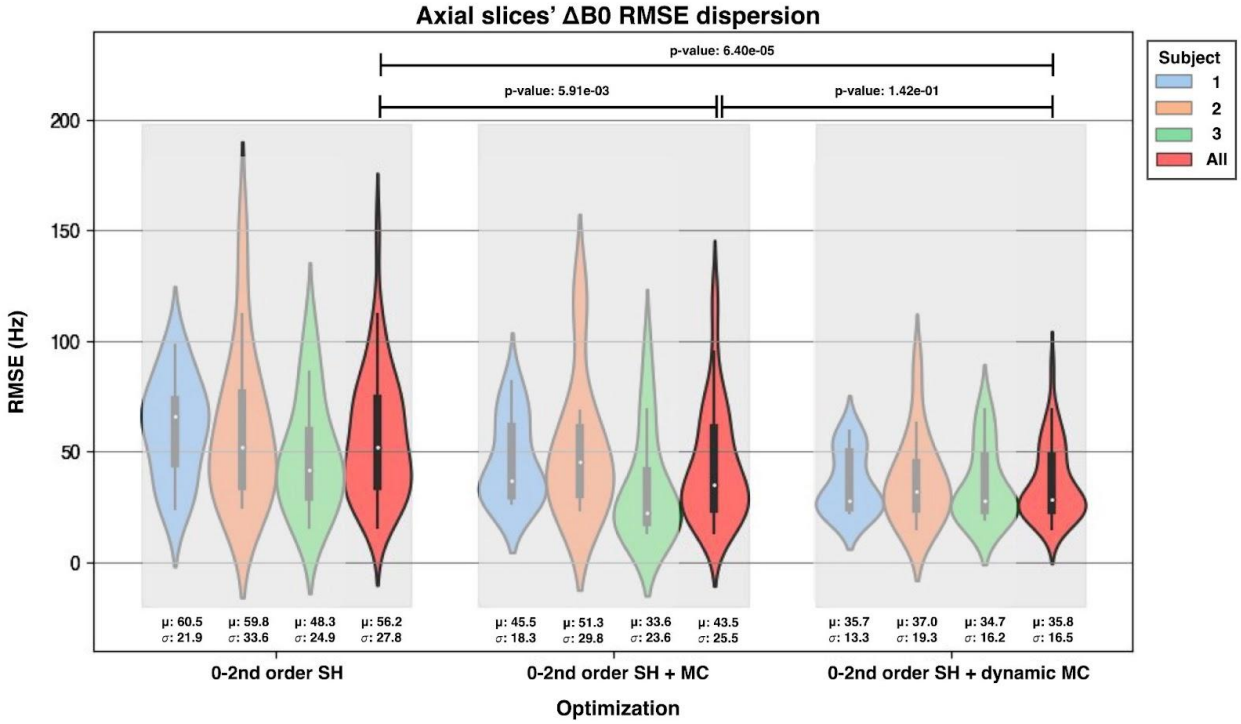

Figure 5.3 Violin plot of ΔB0 resonance offset (y-axis) of all axial slices for three subjects (hue) and three different shim optimizations (x-axis): (i) original acquired field (Baseline), (ii) shimmed field using volume 0-2nd order SH, (iii) shimmed field using volume 15-channel MC + 0-2nd order SH and (iv) shimmed filed using 0-2nd order SH optimization + slice-wise MC optimization. The indicated p-values are from a unilateral Mann-Whitney U test between the different optimizations.

Using the 15-channel AC/DC coil achieved a 22% reduction in B_0 RMSE compared to the baseline acquisition (0-2nd order spherical harmonics) when applying volume-wise shimming, and a 36% reduction when applying slice-wise dynamic shimming. This RMSE reduction corresponded to a 41% decrease in voxel shift in EPIs, alongside substantial signal recovery.

5.4 Signal Recovery in the Brain at 7T

Following the achievement of dynamic slice-wise shimming, the next step was to implement through-slice gradient regularization into the optimization. This new optimization, previously detailed in CHAPTER 4, was first developed during an internship at the Martinos Center, Massachusetts General Hospital (MGH). At the time of writing this thesis, only one successful subject was acquired due to technical issues with the 7T system and the 32-channel

AC/DC coil used in the experiments. Figure 5.4 presents a brain slice acquired at 7T with 2mm isotropic voxels from this subject. In this context, it is important to note that the *w* parameter originates from equation 4.5, where $w = 0$ indicates no through-slice gradient minimization.

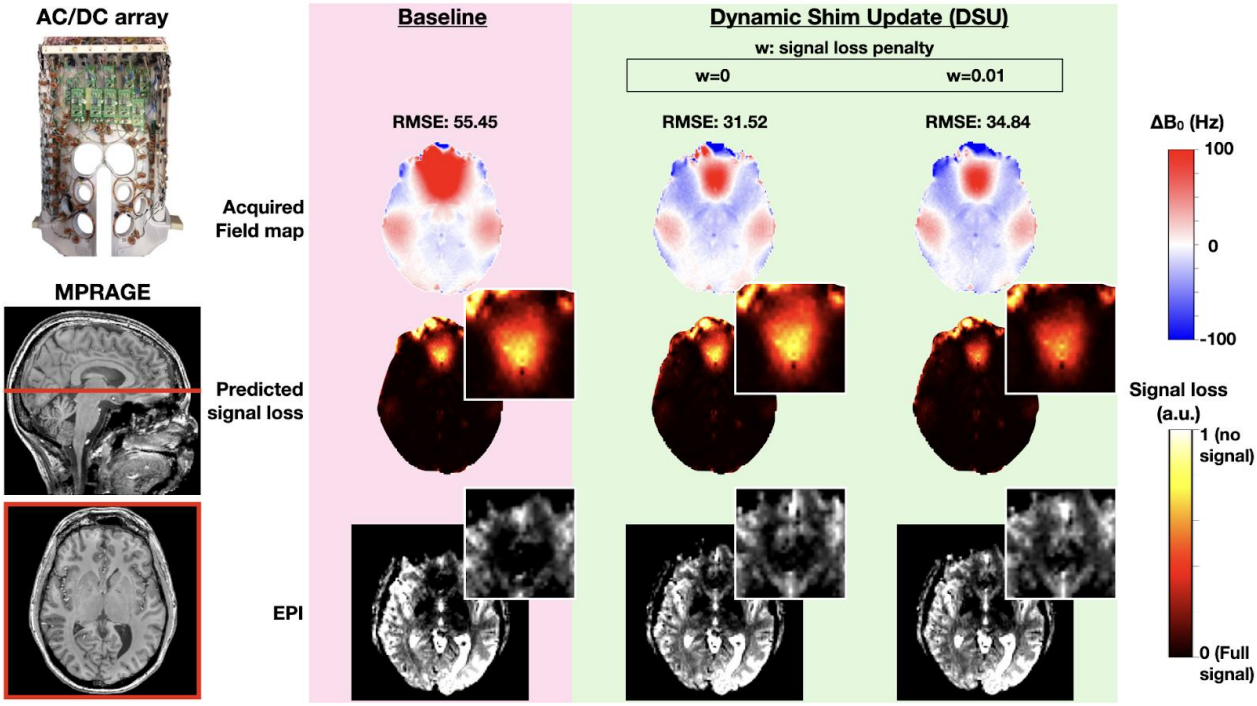

Figure 5.4 MPRAGE, acquired field map, predicted signal loss maps and EPIs (2 mm iso) for one slice of the brain for the baseline and for different signal loss penalty parameters ($w = [0, 0.01]$) from equation 4.5. The signal loss maps were computed using equation 4.3. All optimizations apart from baseline were dynamic shim update (DSU) of the 15-channel coil channels.

As shown in the figure above, brain imaging at 7T demonstrates results comparable to spinal imaging at 3T, with similar B_0 field maps observed between the two *w* parameters. However, incorporating through-slice gradient optimization ($w = 0.01$) yields a significant improvement in the EPI signal compared to traditional in-plane B_0 RMSE minimization alone ($w = 0$). A higher EPI (1 mm iso) signal was also measured in tSNR experiments, as shown in Figure 5.5.

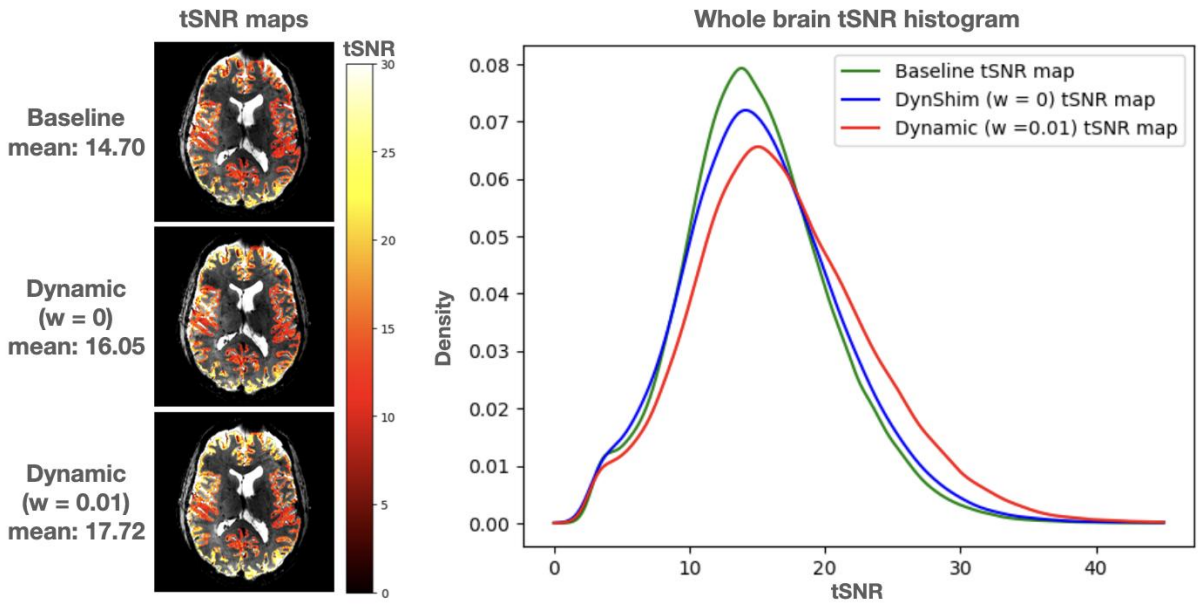

Figure 5.5 tSNR maps in grey matter for one slice of a 1 mm iso GRE-EPI and the tSNR histogram for the whole brain volume for each shimming optimization (w=0 and w=0.01). All optimizations apart from baseline were dynamic shim update (DSU) of the 15-channel coil channels.

As shown in the figure above, signal recovery optimization (w = 0.01) produced a higher tSNR in gray matter, shifting the histogram toward higher values compared to both the baseline acquisition (volume shim using the scanner's 0-2nd order spherical harmonics) and dynamic slice-wise shimming without through-slice gradient minimization (w = 0). Overall, the only subject scanned successfully proved that incorporating through-slice gradient regularization into the least-squares optimization provides significant value in enhancing tSNR in gray matter during a standard fMRI acquisition at 7T.

5.5 Extra discussion on signal recovery

After the paper was submitted, further simulations were run. In these simulations, it was observed that first-order gradients could not recover much signal on their own but were greatly beneficial when combined with the AC/DC coil. From this result, I hypothesize that the gradients are not good at compensating through-slice gradient but help drastically at homogenizing the in-plane field which lets the AC/DC coil further optimize the through-slice gradient. The second-order

spherical harmonics were not simulated for dynamic shimming because they are not made to be updated rapidly and create high eddy currents.

CHAPTER 6 CONCLUSION AND RECOMMENDATIONS

This thesis contributes to spinal cord MRI by implementing and evaluating a dynamic slice-wise shimming approach for GRE-EPI sequences using a 15-channel AC/DC coil, specifically using signal recovery optimization. Dynamic slice-wise shimming, designed to address both in-plane B_0 homogeneity and through-slice gradients, enabled meaningful reductions in signal loss and geometric distortions across cervicothoracic regions. This dual-parameter optimization, tuned to a signal penalty value of $w = 0.01$, yielded a sharp and consistent decrease in B_0 RMSE while also minimizing the through-slice gradient which is directly linked to signal loss. This result was reflected in tSNR studies where tSNR in key areas was significantly enhanced. Notably, T2 showed a 201% mean tSNR improvement, while C3 achieved a 78% improvement—highly impactful results for achieving clearer images in these challenging regions.

Implementing this shimming method was not without significant challenges. The spinal cord is a complex environment for MRI due to its narrow cross-sectional area and surrounding anatomy, which generates strong static B_0 field inhomogeneities. These are further complicated by the spinal cord's location near moving organs, making it vulnerable to field shifts from physiological sources like breathing. Furthermore, high in-plane resolution often necessitates thicker slices to achieve sufficient SNR in GRE-EPI sequences, exacerbating signal loss. Optimizing a method that could simultaneously address in-plane B_0 distortions and through-slice gradients demanded a balance of parameters within the signal recovery optimization model. The results underscore the effectiveness of moderate signal recovery penalties ($w = 0.01$) to limit excessive distortions while preserving signal quality, whereas higher values ($w = 1$) worsened B_0 field uniformity and amplified slice-to-slice variability.

Despite the progress achieved, the study faced notable limitations. In lower spinal cord slices, particularly at T3, severe initial signal loss and non-optimal signal coverage in the region constrained the efficacy of the shimming adjustments, resulting in lower-than-anticipated tSNR improvements. Additionally, attempts to incorporate higher through-slice gradient correction led to significant increases in RMSE and geometric distortions, highlighting the need for a balanced approach that prioritizes moderate, adaptive shim adjustments.

The findings pave the way for future studies, which could enhance this approach by incorporating real-time B_0 adjustments aligned with respiratory cycles to address dynamic field

variations, which induce a time-varying through-slice gradient, without the time penalty (up to three times longer [59]) of respiratory gating. Additionally, this method could be applied to stronger field strengths like McGill's 7T system where signal loss is even more prominent. An identical coil to the one used in this study is available for the 7T and a second shim system is currently being built to run the experiment on the 7T system. This can lead to new and exciting experiments, where a duo-scanner study can be conducted by comparing different acquisitions, field maps, and shimming impacts for two different field strengths (3T and 7T) using a geometrically identical coil. Another potential project is the optimization of a shim coil for the thoracic spinal cord using Pinho Menese et al.'s SVD technique [60] to help shim this difficult region that we observed low signal around the T3 vertebral level in our experiments.

Finally, through open-source implementation and integration with AC/DC coil technology, this work establishes a foundation for continued development and refinement of shimming techniques, fostering further advancements in spinal cord imaging and beyond.

REFERENCES

[1] K. Ong *et al.*, “Detection of subtle white matter lesions in MRI through texture feature extraction and boundary delineation using an embedded clustering strategy,” *Sci. Rep.*, vol. 12, no. 1, p. 4433, Mar. 2022.

[2] A. J. Sim, E. Kaza, L. Singer, and S. A. Rosenberg, “A review of the role of MRI in diagnosis and treatment of early stage lung cancer,” *Clin. Transl. Radiat. Oncol.*, vol. 24, pp. 16–22, Sep. 2020.

[3] B. Hilton *et al.*, “Cord compression defined by MRI is the driving factor behind the decision to operate in Degenerative Cervical Myelopathy despite poor correlation with disease severity,” *PLoS One*, vol. 14, no. 12, p. e0226020, Dec. 2019.

[4] S. Ogawa and T. M. Lee, “Magnetic resonance imaging of blood vessels at high fields: in vivo and in vitro measurements and image simulation,” *Magn. Reson. Med.*, vol. 16, no. 1, pp. 9–18, Oct. 1990.

[5] “Magnetic homogeneity,” *Questions and Answers in MRI*. [Online]. Available: http://mriquestions.com/why-homogeneity.html. [Accessed: 24-Oct-2024].

[6] M. I. Karamat, S. Darvish-Molla, and A. Santos-Diaz, “Opportunities and challenges of 7 Tesla magnetic resonance imaging: A review,” *Crit. Rev. Biomed. Eng.*, vol. 44, no. 1–2, pp. 73–89, 2016.

[7] P. W. Stroman *et al.*, “The current state-of-the-art of spinal cord imaging: methods,” *Neuroimage*, vol. 84, pp. 1070–1081, Jan. 2014.

[8] E. Bercovich and M. C. Javitt, “Medical imaging: From roentgen to the digital revolution, and beyond,” *Rambam Maimonides Med. J.*, vol. 9, no. 4, Oct. 2018.

[9] T. Geva, “Magnetic resonance imaging: historical perspective,” *J. Cardiovasc. Magn. Reson.*, vol. 8, no. 4, pp. 573–580, 2006.

[10] H. Kabasawa, “MR imaging in the 21st century: Technical innovation over the first two decades,” *Magn. Reson. Med. Sci.*, vol. 21, no. 1, pp. 71–82, Mar. 2022.

[11] K. Uğurbil, “Imaging at ultrahigh magnetic fields: History, challenges, and solutions,” *Neuroimage*, vol. 168, pp. 7–32, Mar. 2018.

[12] CEA, “The most powerful MRI scanner in the world delivers its first images!,” Oct. 2021.

[13] “Relaxation time, T1, T2,” *Questions and Answers in MRI*. [Online]. Available: http://mriquestions.com/why-is-t1--t2.html. [Accessed: 28-Aug-2024].

[14] T. Verma and J. Cohen-Adad, “Effect of respiration on the B0 field in the human spinal cord at 3T: Effect of Respiration on B0Field in Human Spinal Cord,” *Magn. Reson. Med.*, vol. 72, no. 6, pp. 1629–1636, Dec. 2014.

[15] S. J. Vannesjo, K. L. Miller, S. Clare, and I. Tracey, “Spatiotemporal characterization of breathing-induced B0 field fluctuations in the cervical spinal cord at 7T,” *Neuroimage*, vol. 167, pp. 191–202, Feb. 2018.

[16] J. Finsterbusch, F. Eippert, and C. Büchel, "Single, slice-specific z-shim gradient pulses improve T2*-weighted imaging of the spinal cord," *Neuroimage,* vol. 59, no. 3, pp. 2307–2315, Feb. 2012.

[17] J. L. Wilson and P. Jezzard, "Utilization of an intra-oral diamagnetic passive shim in functional MRI of the inferior frontal cortex," *Magn. Reson. Med.,* vol. 50, no. 5, pp. 1089–1094, Nov. 2003.

[18] J. L. Wilson, M. Jenkinson, and P. Jezzard, "Optimization of static field homogeneity in human brain using diamagnetic passive shims," *Magn. Reson. Med.,* vol. 48, no. 5, pp. 906–914, Nov. 2002.

[19] J. P. Stockmann and L. L. Wald, "In vivo B0 field shimming methods for MRI at 7T," *Neuroimage,* vol. 168, pp. 71–87, Mar. 2018.

[20] H. P. Hetherington, C. H. Moon, M. Schwerter, N. J. Shah, and J. W. Pan, "Dynamic B0 shimming for multiband imaging using high order spherical harmonic shims," *Magn. Reson. Med.,* vol. 85, no. 1, pp. 531–543, Jan. 2021.

[21] C. Juchem, T. W. Nixon, S. McIntyre, D. L. Rothman, and R. A. de Graaf, "Magnetic field homogenization of the human prefrontal cortex with a set of localized electrical coils," *Magn. Reson. Med.,* vol. 63, no. 1, pp. 171–180, Jan. 2010.

[22] C. Juchem, T. W. Nixon, S. McIntyre, V. O. Boer, D. L. Rothman, and R. A. de Graaf, "Dynamic multi-coil shimming of the human brain at 7T," *J. Magn. Reson.,* vol. 212, no. 2, pp. 280–288, Oct. 2011.

[23] R. Topfer, A. Foias, N. Stikov, and J. Cohen-Adad, "Real-time correction of respiration-induced distortions in the human spinal cord using a 24-channel shim array," *Magn. Reson. Med.,* vol. 80, no. 3, pp. 935–946, Sep. 2018.

[24] J. P. Stockmann *et al.*, "A 31-channel integrated 'AC/DC' B0 shim and radiofrequency receive array coil for improved 7T MRI," *Magn. Reson. Med.,* vol. 87, no. 2, pp. 1074–1092, Feb. 2022.

[25] H. Han, A. W. Song, and T.-K. Truong, "Integrated parallel reception, excitation, and shimming (iPRES): Integrated Parallel Reception, Excitation, and Shimming," *Magn. Reson. Med.,* vol. 70, no. 1, pp. 241–247, Jul. 2013.

[26] J. Cohen-Adad and N. Lopez Rios, "15-channel AC/DC coil design files." Zenodo, 2024.

[27] A. M. Blamire, D. L. Rothman, and T. Nixon, "Dynamic shim updating: a new approach towards optimized whole brain shimming," *Magn. Reson. Med.,* vol. 36, no. 1, pp. 159–165, Jul. 1996.

[28] C. Juchem, S. Umesh Rudrapatna, T. W. Nixon, and R. A. de Graaf, "Dynamic multi-coil technique (DYNAMITE) shimming for echo-planar imaging of the human brain at 7 Tesla," *Neuroimage,* vol. 105, pp. 462–472, Jan. 2015.

[29] A. Aghaeifar *et al.*, "Dynamic B_0 shimming of the human brain at 9.4 T with a 16-channel multi-coil shim setup," *Magn. Reson. Med.,* vol. 80, no. 4, pp. 1714–1725, Oct. 2018.

[30] H. Islam, C. S. W. Law, K. A. Weber, S. C. Mackey, and G. H. Glover, "Dynamic per slice shimming for simultaneous brain and spinal cord fMRI," *Magn. Reson. Med.,* vol. 81, no. 2, pp. 825–838, Feb. 2019.

[31] J. P. Stockmann *et al.*, “A 32-channel combined RF and B0 shim array for 3T brain imaging,” *Magn. Reson. Med.*, vol. 75, no. 1, pp. 441–451, Jan. 2016.

[32] Bréhéret A, D’Astous A,Lopez-Rios N, Alonso-Ortiz E, Stockmann J, and Cohen-Adad J, “Dynamic shimming of the spinal cord using a 15-channel AC/DC coil,” in *Proceedings of the international society for magnetic resonance in medicine, 2024*, Singapour, 2024.

[33] J. D. Cuthbertson, T.-K. Truong, R. Stormont, F. Robb, A. W. Song, and D. Darnell, “An iPRES-W coil array for simultaneous imaging and wireless localized B0 shimming of the cervical spinal cord,” *Magn. Reson. Med.*, vol. 88, no. 2, pp. 1002–1014, Aug. 2022.

[34] T.-K. Truong, D. Darnell, and A. W. Song, “Integrated RF/shim coil array for parallel reception and localized B0 shimming in the human brain,” *Neuroimage*, vol. 103, pp. 235–240, Dec. 2014.

[35] D. Willey, D. Darnell, A. W. Song, and T.-K. Truong, “Application of an integrated radio-frequency/shim coil technology for signal recovery in fMRI,” *Magn. Reson. Med.*, vol. 86, no. 6, pp. 3067–3081, Dec. 2021.

[36] D. K. Overson, D. Darnell, F. Robb, A. W. Song, and T.-K. Truong, “Flexible multi-purpose integrated RF/shim coil array for MRI and localized B0 shimming,” *Magn. Reson. Med.*, vol. 91, no. 2, pp. 842–849, Feb. 2024.

[37] E. Alonso-Ortiz, D. Papp, A. D’Astous, and J. Cohen-Adad, “Dynamic shimming in the cervical spinal cord for multi-echo gradient-echo imaging at 3 T,” *Neuroimage Rep.*, vol. 3, no. 1, p. 100150, Mar. 2023.

[38] F. J. Cooke, A. M. Blamire, D. N. Manners, P. Styles, and B. Rajagopalan, “Quantitative proton magnetic resonance spectroscopy of the cervical spinal cord,” *Magn. Reson. Med.*, vol. 51, no. 6, pp. 1122–1128, Jun. 2004.

[39] F. Giove, G. Garreffa, G. Giulietti, S. Mangia, C. Colonnese, and B. Maraviglia, “Issues about the fMRI of the human spinal cord,” *Magn. Reson. Imaging*, vol. 22, no. 10, pp. 1505–1516, Dec. 2004.

[40] M. Kaptan *et al.*, “Automated slice-specific z-shimming for functional magnetic resonance imaging of the human spinal cord,” *Hum. Brain Mapp.*, vol. 43, no. 18, pp. 5389–5407, Dec. 2022.

[41] Nick Arango, Jason P Stockmann, Thomas Witzel, Lawrence Wald, and Jacob White, “Open-source, low-cost, flexible, current feedback-controlled driver circuit for local B0 shim coils and other applications,” in *International Society for Magnetic Resonance in Medicine*, Singapore, 2016.

[42] J. Cohen-Adad, “Functional magnetic resonance imaging of the spinal cord: Current status and future developments,” *Semin. Ultrasound CT MR*, vol. 38, no. 2, pp. 176–186, Apr. 2017.

[43] C. S. Aigner, M. F. Sánchez Alarcon, A. D’Astous, E. Alonso-Ortiz, J. Cohen-Adad, and S. Schmitter, “Calibration-free parallel transmission of the cervical, thoracic, and lumbar spinal cord at 7T,” *Magn. Reson. Med.*, vol. 92, no. 4, pp. 1496–1510, Oct. 2024.

[44] R. Topfer *et al.*, “A 24-channel shim array for the human spinal cord: Design, evaluation, and application,” *Magn. Reson. Med.*, vol. 76, no. 5, pp. 1604–1611, Nov. 2016.

[45] Y. Chu, B. Fricke, and J. Finsterbusch, “Improving T2*-weighted human cortico-spinal acquisitions with a dedicated algorithm for region-wise shimming,” *Neuroimage*, vol. 268, no. 119868, p. 119868, Mar. 2023.

[46] S. McElroy *et al.*, “Integrated slice-specific dynamic shimming for whole-body diffusion-weighted MR imaging at 1.5 T,” *MAGMA*, vol. 34, no. 4, pp. 513–521, Aug. 2021.

[47] J. Finsterbusch, C. Sprenger, and C. Büchel, “Combined T2*-weighted measurements of the human brain and cervical spinal cord with a dynamic shim update,” *Neuroimage*, vol. 79, pp. 153–161, Oct. 2013.

[48] N. L. Rios *et al.*, “Integrated AC/DC coil and dipole Tx array for 7T MRI of the spinal cord,” in *Proc ISMRM*, 2019, vol. 27, p. 220.

[49] J. Finsterbusch and Y. Chu, “Simultaneous multislice imaging with slice-specific z-shim,” *Magn. Reson. Med.*, vol. 90, no. 2, pp. 633–642, Aug. 2023.

[50] D. Tsivaka *et al.*, “A second-order and slice-specific linear shimming technique to improve spinal cord fMRI,” *Magn. Reson. Imaging*, vol. 102, pp. 151–163, Oct. 2023.

[51] Finsterbusch J., “On z-shimming: settings maximizing the signal amplitude may not be derivable from the linear field component and may depend on the echo time,” in *Proceedings of the international society for magnetic resonance in medicine, 2024*, Singapour, 2024.

[52] A. D’Astous *et al.*, “Shimming toolbox: An open-source software toolbox for B0 and B1 shimming in MRI,” *Magn. Reson. Med.*, vol. 89, no. 4, pp. 1401–1417, Apr. 2023.

[53] C. Juchem, T. W. Nixon, P. Diduch, D. L. Rothman, P. Starewicz, and R. A. de Graaf, “Dynamic Shimming of the Human Brain at 7 Tesla,” *Concepts Magn. Reson. Part B Magn. Reson. Eng.*, vol. 37B, no. 3, pp. 116–128, Jul. 2010.

[54] B. De Leener *et al.*, “SCT: Spinal Cord Toolbox, an open-source software for processing spinal cord MRI data,” *Neuroimage*, vol. 145, no. Pt A, pp. 24–43, Jan. 2017.

[55] S. M. Dupont *et al.*, “Fully-integrated framework for the segmentation and registration of the spinal cord white and gray matter,” *Neuroimage*, vol. 150, pp. 358–372, Apr. 2017.

[56] E. N. Karthik, S. Bedard, J. Valosek, S. Chandar, and J. Cohen-Adad, “Contrast-agnostic Spinal Cord Segmentation: A Comparative Study of ConvNets and Vision Transformers,” *https://openreview.net/*, Medical Imaging with Deep Learning 2024, 2024.

[57] M. Jenkinson, C. F. Beckmann, T. E. J. Behrens, M. W. Woolrich, and S. M. Smith, “FSL,” *Neuroimage*, vol. 62, no. 2, pp. 782–790, Aug. 2012.

[58] P. Virtanen *et al.*, “SciPy 1.0: fundamental algorithms for scientific computing in Python,” *Nat. Methods*, vol. 17, no. 3, pp. 261–272, Mar. 2020.

[59] “Gating methods,” *Questions and Answers in MRI*. [Online]. Available: http://mriquestions.com/gating-methods.html. [Accessed: 25-Jan-2025].

[60] B. Pinho Meneses *et al.*, “Shim coils tailored for correcting B0 inhomogeneity in the human brain (SCOTCH): Design methodology and 48-channel prototype assessment in 7-Tesla MRI,” *Neuroimage*, vol. 261, no. 119498, p. 119498, Nov. 2022.